CHALMERS
UNIVERSITY OF TECHNOLOGY

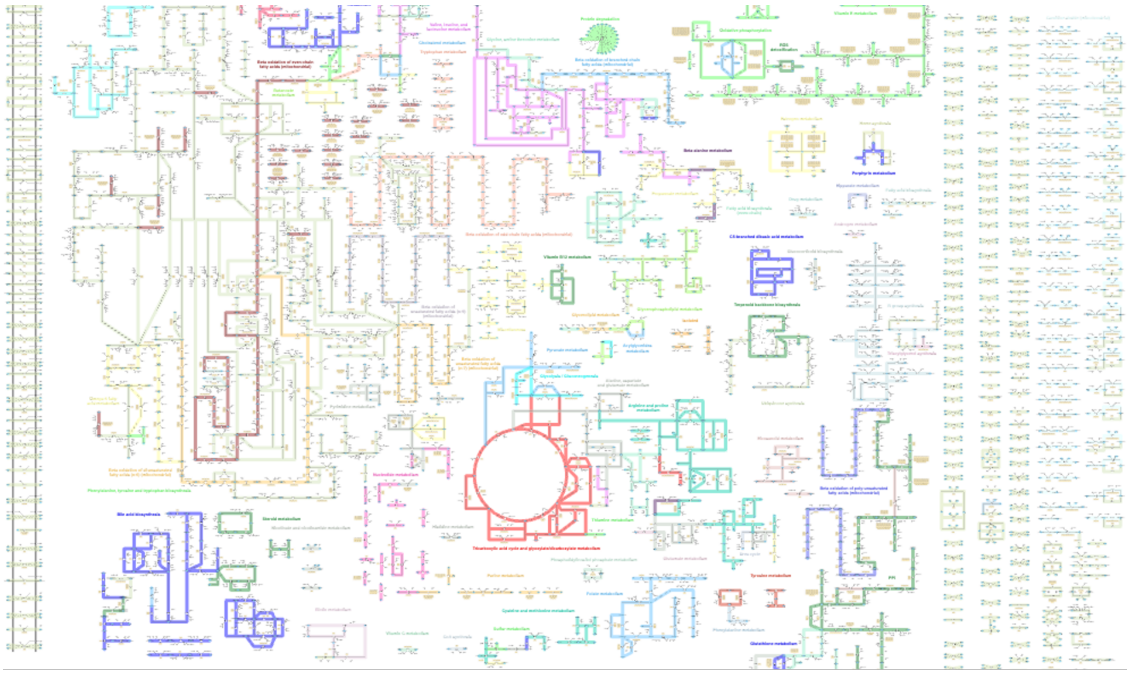

A Patient-Specific Metabolic Modeling Framework of Whole-Blood Transcriptomes for Early Screening of Prodromal Parkinson's Disease

Master's thesis in Biotechnology

HAILEY CHAPMAN

DEPARTMENT OF LIFE SCIENCE

CHALMERS UNIVERSITY OF TECHNOLOGY
Gothenburg, Sweden 2026
www.chalmers.se

Master's thesis 2026

A Patient-Specific Metabolic Modeling Framework of Whole-Blood Transcriptomes for Early Screening of Prodromal Parkinson's Disease

Hailey Chapman

CHALMERS
UNIVERSITY OF TECHNOLOGY

Department of Life Science
Division of Systems and Synthetic Biology
Chalmers University of Technology
Gothenburg, Sweden 2026

A Patient-Specific Metabolic Modeling Framework of Whole-Blood Transcriptomes for Early Screening of Prodromal Parkinson's Disease
HAILEY CHAPMAN

Supervisor: Eduard Kerkhoven, Department of Life Science
Examiner: Annikka Polster, Department of Life Science

Master's Thesis 2026
Department of Life Science
Division of Systems and Synthetic Biology
Chalmers University of Technology
SE-412 96 Gothenburg
Telephone +46 31 772 1000

Typeset in LaTeX
Printed by Chalmers Reproservice
Gothenburg, Sweden 2026

Abstract

Parkinson's disease (PD) is a progressive neurodegenerative disorder associated with widespread metabolic dysfunction, particularly involving mitochondrial pathways. Because clinical diagnosis typically occurs only after substantial neuronal loss has already occurred, there is increasing interest in identifying molecular alterations associated with the prodromal phase of disease progression. Genome-scale metabolic models (GEMs) provide a systems-level framework for integrating transcriptomic data with known metabolic networks to investigate disease-associated metabolic changes.

In this thesis, the mitochondrial compartment of HumanGEM was first curated through systematic comparison with the manually curated MitoCore model to improve reaction directionality and compartment consistency. Longitudinal whole-blood RNA-seq data from healthy control, prodromal PD, and established PD cohorts were then integrated with the curated model using the ftINIT contextualization algorithm to generate 2326 patient-specific GEMs. Flux sampling was subsequently performed to characterize feasible metabolic states across patient-specific models.

Global analyses of model structure and sampled flux-space organization revealed limited disease separation at the systems level. However, differential flux analysis identified metabolic alterations. Significant reactions were associated with multiple pathways that have been previously implicated in PD, such as amino acid metabolism, lysosomal degradation and fatty acid processing.

Overall, this work demonstrates the application of patient-specific metabolic modeling to investigate systemic metabolic alterations associated with Parkinson's disease progression. Although the identified metabolic differences were modest and heterogeneous across longitudinal timepoints, the findings demonstrate the utility of GEM-based approaches for exploratory systems-level analysis of complex human disease.

Keywords: Genome Scale Model, Prodromal Parkinson's Disease, Differential Flux Analysis, Mitochondrial Metabolism, Patient-Specific Modeling

Acknowledgements

I would like to sincerely thank my supervisor, Eduard Kerkhoven, and my examiner, Annikka Polster, for giving me the opportunity to work on this project and for their invaluable guidance, support, and expertise throughout this thesis. Their insight and encouragement were instrumental to both the scientific work and my personal development as a researcher.

I would also like to thank everyone in Ed and Annikka's research groups for creating such a collaborative and supportive environment. In particular, I am deeply grateful to Fabian Moreno Avitia for his patience, wisdom, and the time and support he provided throughout this project. I would also like to thank Danish Anwer for his previous work and continued support, as well as Giovanni Perra for the many helpful discussions and for always being willing to bounce around ideas.

Finally, I would like to thank my family, friends, and those closest to me for their encouragement and support throughout my studies and during my thesis.

Hailey Chapman

List of Acronyms

Below is the list of acronyms that have been used throughout this thesis listed in alphabetical order:

ACHR	Artificial Centering Hit-and-Run
ATP	Adenosine Triphosphate
BL	Baseline
DA	Dopaminergic
DFA	Differential Flux Analysis
EC	Enzyme Commission
FBA	Flux Balance Analysis
FDR	False Discovery Rate
ftINIT	Fast task-driven Integrative Network Inference for Tissues
FVA	Flux Variability Analysis
GEM	Genome-Scale Metabolic Model
GPR	Gene-Protein-Reaction
ISR	Integrated Stress Response
KEGG	Kyoto Encyclopedia of Genes and Genomes
PCA	Principal Component Analysis
PD	Parkinson's Disease
PPMI	Parkinson's Progression Markers Initiative
RNA-seq	RNA Sequencing
ROS	Reactive Oxygen Species
SNc	Substantia nigra pars compacta
tSNE	t-distributed stochastic neighbor embedding
TPM	Transcripts Per Million
Y1	Year 1
Y2	Year 2
Y3	Year 3
$\Delta_r G'_m$	Transformed Gibbs Free Energy of Reaction

Contents

1

Introduction

Neurodegenerative diseases represent a growing global health challenge due to aging populations, increasing life expectancy, and the absence of curative treatments for many disorders. Among these diseases, Parkinson's disease (PD) has emerged as one of the fastest-growing neurological disorders worldwide, with rising prevalence and substantial societal and clinical burden [1]. Understanding the molecular mechanisms underlying PD progression and identifying early disease-associated alterations remain major challenges in the development of effective diagnostic and therapeutic strategies.

1.1 Parkinson's Disease

This section introduces the clinical and biological background of Parkinson's disease relevant to this thesis, with emphasis on disease progression, metabolic dysfunction, and the challenges associated with early diagnosis.

1.1.1 Clinical and Biological Background

Parkinson's disease (PD) is a progressive neurodegenerative disorder and the second most common neurodegenerative disease worldwide after Alzheimer's disease [1]. During the past several decades, the global prevalence of PD has increased substantially, likely due to aging populations and increasing life expectancy [1]. This growing prevalence has contributed to an increasing clinical and societal burden, emphasizing the need for improved understanding of disease mechanisms and the development of more effective therapeutic strategies.

Clinically, PD is characterized by a combination of motor and non-motor symptoms. The classical motor symptoms include bradykinesia, resting tremor, rigidity, and postural instability, while non-motor manifestations may include constipation, sleep disturbances, cognitive impairment, mood disorders, and hyposmia [2, 3]. Neuropathologically, PD is primarily associated with the progressive degeneration of dopaminergic (DA) neurons within the substantia nigra pars compacta, resulting in reduced dopamine signaling within motor control pathways [3, 4]. The disease is also characterized by the accumulation of misfolded α-synuclein aggregates in the form of Lewy bodies and Lewy neurites, which are thought to contribute to neuronal

dysfunction and degeneration [5].

Despite extensive research efforts, there are currently no disease-modifying therapies capable of halting or reversing PD progression [6]. Existing treatments primarily focus on symptomatic management and are typically initiated only after substantial neuronal degeneration has already occurred [3, 7]. Importantly, PD is highly heterogeneous, with considerable variability in symptom presentation, progression rate, molecular pathology, and treatment response between patients [8]. This heterogeneity complicates both diagnosis and therapeutic development, and highlights the need for improved biomarkers and systems-level approaches capable of identifying early disease-associated molecular alterations.

1.1.2 Disease Progression

PD progression is typically divided into several stages, including a prolonged prodromal phase that precedes the onset of classical motor symptoms [9]. During this early stage, individuals may exhibit a range of non-motor symptoms such as constipation, sleep disturbances, depression, anxiety, and hyposmia [2, 9]. These symptoms can emerge decades before clinical diagnosis and are thought to reflect early neurodegenerative and molecular changes occurring prior to overt motor dysfunction [7, 10].

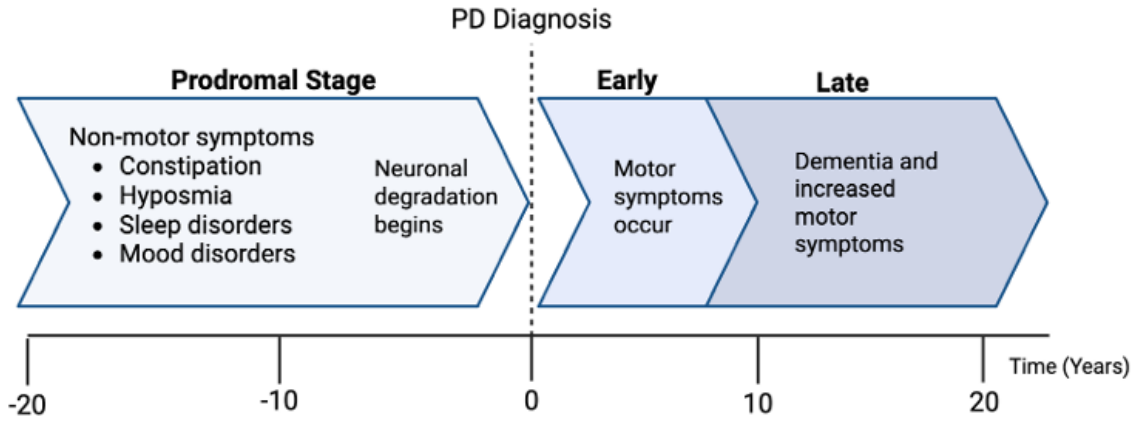

Figure 1.1: ***Parkinson's Disease Progression***

Although PD is clinically diagnosed based primarily on motor symptoms including bradykinesia, rigidity, and resting tremor, substantial degeneration of DA neurons has often already occurred by the time these symptoms become apparent [2, 7]. Previous studies have estimated that a large proportion of dopaminergic neuronal terminals and a significant number of DA neurons within the substantia nigra pars compacta are already lost at the time of diagnosis [10]. Consequently, the prodromal phase is considered a critical window for therapeutic intervention, during which early detection and treatment may have the greatest potential to slow disease progression before extensive irreversible neurodegeneration has occurred [3].

A major challenge is accurately identifying individuals during this stage, before motor symptoms occur. Prodromal symptoms are highly heterogeneous and can

overlap with those of other age-related conditions, making early diagnosis difficult using conventional clinical approaches alone [8, 2]. As a result, there is substantial interest in identifying molecular biomarkers and systems-level alterations associated with early disease progression that may enable earlier diagnosis.

1.1.3 Mitochondrial Dysfunction and Metabolism

Mitochondrial dysfunction is widely recognized as a central hallmark of PD and is thought to play a major role in both neuronal degeneration and disease progression [11, 12]. Mitochondria are essential for cellular energy production, calcium homeostasis, reactive oxygen species (ROS) regulation, and apoptotic signaling, making neuronal populations with high energetic demands particularly vulnerable to mitochondrial impairment. Multiple lines of evidence, including genetic studies, toxin-based models, and post-mortem analyses, have implicated mitochondrial abnormalities as key contributors to PD pathogenesis [11, 13].

One of the earliest and most extensively studied mitochondrial defects in PD is impairment of mitochondrial complex I, a component of the electron transport chain responsible for oxidative phosphorylation [13]. Reduced complex I activity has been consistently observed in PD patient tissues and experimental models, leading to impaired ATP production and increased generation of reactive oxygen species [11]. Elevated oxidative stress can subsequently damage proteins, lipids, and nucleic acids, further contributing to cellular dysfunction and neuronal degeneration. In addition, mutations in several PD-associated genes, including *PINK1*, *Parkin*, and *DJ-1*, are linked to mitochondrial quality control pathways such as mitophagy, further supporting a central role for mitochondrial dysfunction in disease progression [14, 15, 16].

Because PD involves widespread alterations across interconnected metabolic and cellular pathways, systems-level approaches are increasingly important for understanding disease-associated metabolic dysfunction. Metabolic processes such as energy production, amino acid metabolism, lipid metabolism, and oxidative stress responses are highly interconnected and cannot easily be interpreted in isolation. Genome-scale metabolic models (GEMs) provide a framework for studying these interactions by integrating biochemical knowledge with high-throughput omics data into a systems-level representation of cellular metabolism. Such approaches may help identify metabolic alterations associated with early disease progression and provide insight into pathways involved in prodromal PD.

1.2 Metabolic Modeling

This section introduces the computational and modeling framework used in the study, including the principles of genome-scale metabolic modeling and constraint-based analysis, as well as approaches used to generate and analyze patient-specific metabolic models.

1.2.1 Genome-Scale Metabolic Models (GEMs)

Genome-scale metabolic models (GEMs) are computational reconstructions of cellular metabolism that represent the collection of known metabolic reactions encoded by an organism's genome. These models integrate information on genes, proteins, metabolites, and biochemical reactions into a mathematically structured network that can be used to investigate metabolic behavior under different biological conditions [17]. GEMs have become important tools in systems biology, biotechnology, metabolic engineering, and the analysis of cellular physiology in microbial organisms [18]. In human systems, GEMs provide a systems-level framework for studying the complex interactions between metabolic pathways and their relationship to physiology and disease.

Within a GEM, metabolites are connected through enzyme-catalyzed reactions organized into a stoichiometric network [19]. This network is represented mathematically by a stoichiometric matrix, commonly denoted as S, in which rows correspond to a unique metabolite and columns correspond to reactions. Each matrix element represents the stoichiometric coefficient of a metabolite within a given reaction, with negative values corresponding to reactants and positive values corresponding to products. Together, the stoichiometric matrix defines the structure and connectivity of the metabolic network.

A key feature of GEMs is the incorporation of gene–protein–reaction (GPR) associations, which link metabolic reactions to the genes encoding the associated proteins. GPR relationships allow transcriptomic or genomic data to be integrated into metabolic networks by associating gene activity with reaction presence or activity constraints [17]. This enables the generation of context-specific or patient-specific models that better reflect the metabolic capabilities of individual tissues, patients, cell types, or disease states.

1.2.2 Constraint-Based Modeling

Constraint-based modeling is a mathematical framework used to analyze the behavior of genome-scale metabolic networks under a defined set of physicochemical and biological constraints. Rather than requiring detailed kinetic parameters for every reaction, constraint-based approaches restrict the possible reaction fluxes within a network according to stoichiometric relationships, reaction thermodynamics, and upper and lower flux bounds. These approaches are particularly useful for large-scale metabolic systems where kinetic information is often incomplete or unavailable.

A central assumption in many constraint-based methods is the steady-state assumption, in which intracellular metabolite concentrations are assumed to remain approximately constant over time. Under this assumption, the total production and consumption of each metabolite must balance, resulting in the mass balance equation:

$$Sv = 0$$

where S represents the stoichiometric matrix and v represents the vector of reaction fluxes. Additional constraints are imposed through upper and lower reaction bounds:

$$v_{min} \leq v \leq v_{max}$$

which define the allowable range of flux through each reaction based on thermodynamic directionality, enzyme capacity, or biological assumptions.

Together, these constraints define a feasible solution space containing all flux distributions that satisfy the imposed network conditions. Because metabolic networks are highly interconnected and underdetermined, many alternative flux distributions may satisfy the same constraints simultaneously. Constraint-based modeling approaches therefore aim to characterize or analyze this feasible solution space in order to investigate metabolic capabilities, pathway utilization, and disease-associated metabolic behavior.

By adjusting constraints on a GEM, models can be tuned to control for thermodynamics, environmental characteristics, nutrient availability, tissue-specific properties or gene expression.

1.2.3 Flux Space Analysis and Simulations

Constraint-based metabolic models typically admit many feasible steady-state flux distributions that satisfy the imposed network constraints. Many computational approaches have been developed to investigate the properties of this feasible solution space and characterize metabolic behavior under different conditions.

Flux Balance Analysis

One of the most widely used approaches is flux balance analysis (FBA), which identifies an optimal flux distribution by maximizing or minimizing a specified objective function subject to the network constraints [19, 20]. FBA predicts the distribution of metabolic fluxes through the network that best satisfies the defined objective while remaining consistent with the imposed stoichiometric and physicochemical constraints. As a result, FBA can be used to investigate pathway utilization, metabolic capabilities, and the effects of environmental or genetic perturbations on cellular metabolism. However, the biological relevance of FBA predictions depends heavily on the selection of an appropriate objective function.

In microbial systems, objective functions frequently represent biomass production or growth optimization. However, defining biologically meaningful objective functions in human metabolism is substantially more challenging because mammalian cells do not optimize a single universal process [21].

Flux Variability Analysis

Flux variability analysis (FVA) extends FBA by determining the minimum and maximum allowable flux through each reaction while maintaining feasibility under the imposed constraints [22, 23]. Rather than identifying a single optimal solution, FVA characterizes the range of feasible fluxes compatible with the metabolic network and objective constraints.

Flux Sampling

Because many alternative flux distributions may satisfy the same constraints, flux sampling approaches have been developed to more comprehensively explore the feasible solution space. Flux sampling generates large numbers of feasible flux distributions without requiring optimization toward a single objective function [22]. This enables characterization of the broader distribution of possible metabolic states within a model.

There are many different algorithms for flux sampling. In this project, flux sampling was performed using the Artificial Centering Hit-and-Run (ACHR) algorithm. ACHR is a Markov chain Monte Carlo sampling approach designed to uniformly explore the feasible flux space of genome-scale metabolic models while satisfying stoichiometric and flux constraints [24].

Differential Flux Analysis

Following flux sampling, differential flux analysis (DFA) can be performed to identify reactions exhibiting altered flux distributions between biological conditions or patient groups [25]. By comparing sampled flux distributions across disease states, DFA enables identification of metabolic pathways potentially associated with disease progression and provides a framework for investigating metabolic alterations in complex human disorders such as PD.

1.2.4 Human Metabolic Models

Several genome-scale reconstructions of human metabolism have been developed to provide comprehensive representations of metabolic processes across human tissues and cell types. These human metabolic models integrate biochemical knowledge from curated databases, literature sources, and experimental evidence into large-scale metabolic networks suitable for computational analysis [26, 27, 28].

HumanGEM is a comprehensive genome-scale metabolic reconstruction of human metabolism developed by the Systems Biology group at Chalmers University of Technology [26]. The model was generated through integration of several previous human metabolic reconstructions, including HMR [27], and Recon3D [29, 28] using automated reconstruction approaches followed by extensive manual refinement and validation. HumanGEM contains thousands of metabolic reactions distributed across multiple subcellular compartments and incorporates extensive gene–protein–reaction annotations [26].

Although HumanGEM has undergone extensive manual curation, the mitochondrial compartment has not previously been subjected to a focused, systematic consistency check regarding individual reaction localization and directionality. Given the central role of mitochondria in cellular energy metabolism and PD disease progression, accurate representation of mitochondrial reactions is critical.

Importantly, HumanGEM is maintained as a continuously evolving community-driven resource, with ongoing updates and refinements contributed through a version-controlled GitHub repository [30]. This iterative development process allows the model to be continuously improved as new biochemical knowledge and experimental evidence become available. Although HumanGEM provides a broad representation of human metabolic capabilities, not all reactions are active in every biological context. Different tissues, disease states, and physiological conditions exhibit distinct patterns of metabolic activity and gene expression. Consequently, HumanGEM can be further contextualized using omics data to generate models that more accurately reflect specific biological systems.

1.2.5 Patient-Specific GEMs

Patient-specific GEMs are context-specific metabolic models generated by integrating patient-derived omics data with a generic metabolic reconstruction. These approaches aim to tailor the metabolic network to better represent the metabolic capabilities of an individual biological sample or disease state. Transcriptomic integration methods are commonly used to incorporate gene expression data into GEMs by retaining reactions supported by expression evidence while removing or constraining reactions with limited support [31].

One such method for transcriptomic integration is ftINIT [32]. ftINIT is a task-driven contextualization approach that integrates transcriptomic data with a reference metabolic model while simultaneously preserving essential metabolic functionality. Reactions supported by gene expression evidence are preferentially retained, whereas unsupported reactions may be removed unless required to satisfy predefined metabolic tasks. This enables the generation of metabolically functional yet transcriptomically constrained models representing individual patient samples.

The integration of transcriptomic data with GEMs enables systems-level investigation of metabolic alterations associated with disease progression. Rather than analyzing isolated genes or pathways independently, patient-specific GEMs allow metabolic behavior to be evaluated within the context of the broader metabolic network. Such approaches have increasing relevance in systems medicine and personalized medicine, where computational models may help identify disease-associated metabolic alterations, characterize patient heterogeneity, and support the development of individualized therapeutic strategies. Many of these applications are especially promising in a complex, heterogeneous disease such as PD.

1.3 Aims

The overall goal of this thesis was to investigate whether patient-specific GEMs generated from whole-blood RNA-sequencing data could be used to identify metabolic alterations associated with the prodromal PD. This project aimed to explore whether flux-space analysis of patient-specific GEMs could provide insight into disease-associated metabolic changes with potential relevance for early diagnosis and biomarker discovery. To achieve this goal, the project was divided into the following three sub-aims:

Aim 1: Curation of the mitochondrial compartment of HumanGEM

The first aim of this thesis was to evaluate and refine the mitochondrial compartment of HumanGEM through systematic comparison with the manually curated MitoCore model. Reaction reversibility and subcellular localization were assessed to improve biochemical consistency while preserving overall model functionality.

Aim 2: Generation of patient-specific GEMs from whole-blood transcriptomic data

The second aim of this thesis was to integrate longitudinal whole-blood transcriptomic data with HumanGEM to generate patient-specific GEMs representing healthy, prodromal PD, and PD cohorts. These models were used to investigate metabolic network structure and feasible flux-space behavior across disease states and longitudinal timepoints.

Aim 3: Identification of metabolic alterations associated with prodromal PD

The third aim of this thesis was to identify metabolic alterations associated with the prodromal phase of PD through differential flux analysis of patient-specific GEMs. By comparing sampled flux distributions between diagnosis groups, this aim sought to investigate whether patient-specific metabolic modeling could detect pathway-level metabolic changes associated with early disease progression.

2

HumanGEM Curation

2.1 Methods

Although HumanGEM has undergone extensive curation and refinement, the mitochondrial compartment had not previously been subjected to a focused evaluation of reaction localization and directionality consistency. Given the central role of mitochondria in cellular energy metabolism and Parkinson's disease progression, accurate representation of mitochondrial reactions was considered particularly important for downstream patient-specific metabolic modeling.

To evaluate mitochondrial consistency within HumanGEM, reactions were systematically compared against MitoCore, a manually curated metabolic model focused on central and mitochondrial metabolism [33]. MitoCore prioritizes biochemical accuracy and thermodynamic consistency over network breadth, making it a suitable reference framework for evaluating mitochondrial reactions in HumanGEM.

2.1.1 Matching Model Reactions

Filtering of non-informative reactions

To start comparison between models, reactions needed to be matched between the two models so that mismatches in reversibility and compartments could be identified. Prior to reaction matching, the MitoCore reaction list was filtered to exclude reactions that are not informative for validating core mitochondrial biochemistry in HumanGEM. Specifically, transport reactions and boundary condition reactions were removed from the MitoCore reference set. HumanGEM already contains an extensive set of transport and exchange reactions that do not require further curation. MitoCore's transport and boundary reactions were identified based on model annotations.

Stepwise reaction matching and verification

Because HumanGEM and MitoCore were developed independently, the two models use distinct naming conventions for metabolites and reactions. However, both models provide cross-references to external biochemical databases, including KEGG and BiGG, which enable systematic comparison.

Following filtering, MitoCore reactions were matched to HumanGEM reactions using a stepwise identifier-based approach. Reactions were first matched using shared BiGG identifiers, followed by KEGG reaction identifiers for reactions that remained unmatched after the initial matching pass. For remaining reactions lacking consistent database identifiers, potential matches were identified using shared Enzyme Commission (EC) numbers and manually evaluated based on reaction stoichiometry.

In cases where multiple HumanGEM reactions were potential matches for a single MitoCore reaction (e.g. due to compartmental duplication), candidates were reviewed manually, and preference was given to reactions with consistent mitochondrial localization. All matching steps were tracked in a structured match ledger to ensure transparency and reproducibility.

Assessment of reaction directionality and compartment consistency

For each matched reaction pair, reaction reversibility and subcellular localization were compared between MitoCore and HumanGEM. Directionality consistency was assessed based on reaction bounds, and reactions were flagged when reversibility differed between the two models. Subcellular localization was evaluated by comparing compartment assignments, with HumanGEM intermembrane space reactions treated as mitochondrial for consistency with the MitoCore compartment definition.

Each matched reaction was annotated with flags indicating whether reaction directionality and compartment localization were consistent between models. Reactions present in MitoCore but lacking a corresponding mitochondrial reaction in HumanGEM were recorded as missing. These annotations formed the basis for downstream evaluation of mitochondrial representation in HumanGEM.

2.1.2 Decision framework for model updates

Following reaction matching, a structured decision framework was applied to determine whether and how HumanGEM reactions should be modified to improve consistency with MitoCore. This framework was designed to ensure that changes were applied conservatively, based on biochemical evidence, and without compromising global model functionality.

The decision framework used reaction-level annotations generated during matching, including flags indicating mismatches in reaction reversibility, subcellular localization, or reaction presence. Reactions were grouped into categories reflecting agreement, disagreement, or absence between the two models.

The decision logic is shown in Figure 2.1, with detailed decision paths for each category described below.

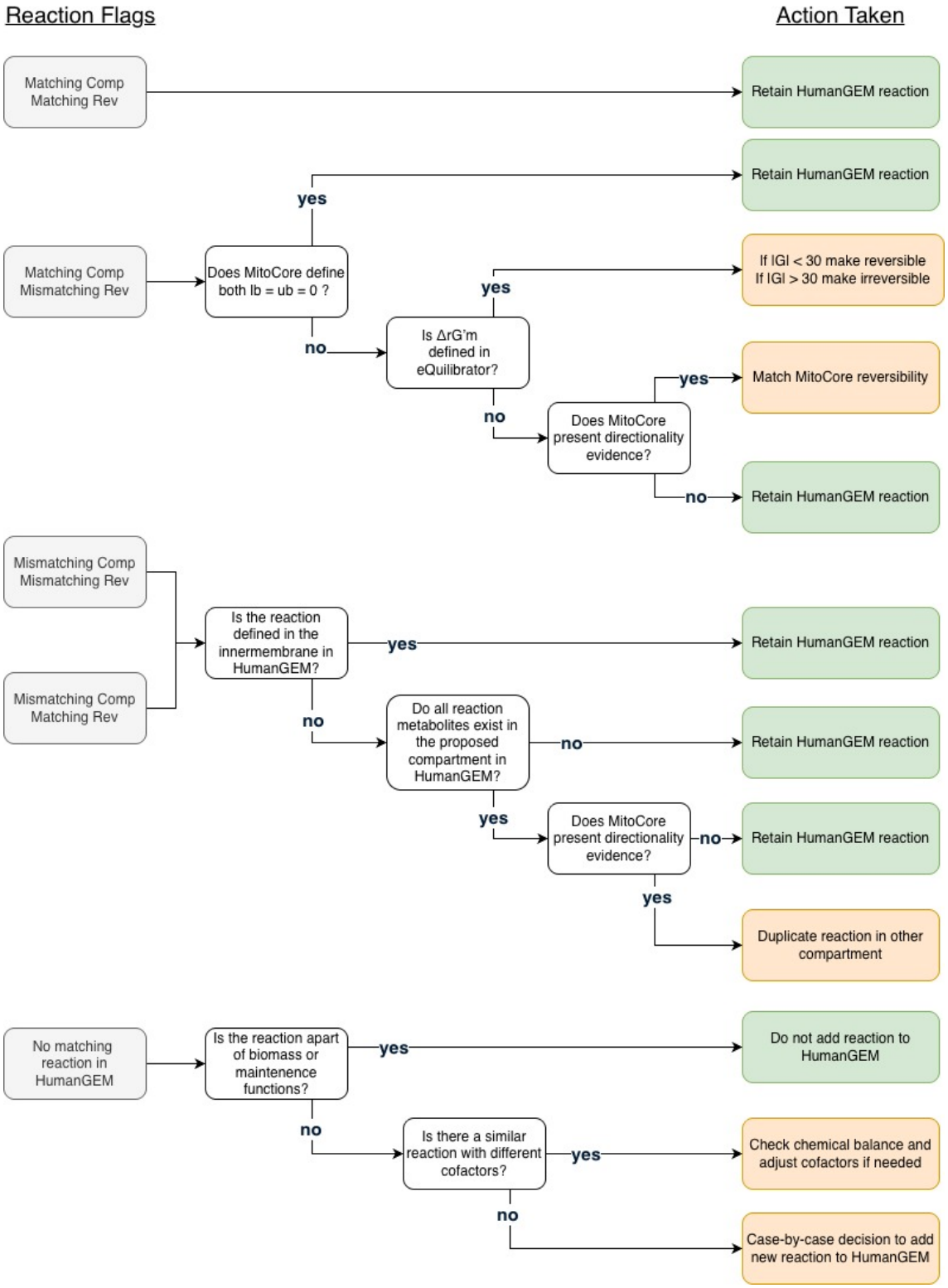

Figure 2.1: ***Decision framework for reaction curation in HumanGEM.*** *A structured decision tree used to determine whether and how reactions in HumanGEM were modified to improve consistency with MitoCore. Reactions were first categorized based on agreement or disagreement in subcellular compartment localization (comp) and reaction reversibility (rev). For reactions with reversibility discrepancies, thermodynamic evidence was evaluated using estimates of the transformed Gibbs free energy of reaction ($\Delta_r G'_m$) obtained from eQuilibrator, where available [34]. Terminal nodes indicate the resulting curation action applied to each reaction.*

2.2 Results

2.2.1 Alterations to HumanGEM

Reversibility discrepancies between HumanGEM and MitoCore

Comparison of mitochondrial reactions between HumanGEM and MitoCore identified a subset of reactions for which reaction reversibility differed between the two models.

Application of the decision framework (Figure 2.1) resulted in proposed updates to reaction bounds for 39 mitochondrial reactions. For reactions with available thermodynamic information (38 of the proposed reactions), estimates of the transformed Gibbs free energy of reaction ($\Delta_r G'_m$) obtained from eQuilibrator were used to assess the plausibility of reversibility. Reactions with $|\Delta_r G'_m| > 30$ kJ mol^{-1} were constrained to be irreversible, whereas reactions with $|\Delta_r G'_m| \leq 30$ kJ mol^{-1} were retained or set as reversible.

In the case where thermodynamic estimates were unavailable, reaction directionality was evaluated based on biochemical evidence reported in MitoCore and associated database references. Using this combined approach, reaction bounds in HumanGEM were updated to improve consistency with established mitochondrial biochemistry while preserving model feasibility. A summary of reactions with updated bounds is provided in Appendix Table A.1.

Compartment localization discrepancies and reaction duplication

In addition to reversibility differences, comparison with MitoCore revealed a small set of reactions with inconsistent subcellular localization between the two models. For these reactions, MitoCore annotated the corresponding enzymes as mitochondrial, and independent localization evidence from MitoCarta supported mitochondrial presence.

Rather than altering or removing existing reactions in HumanGEM, these discrepancies were resolved by duplicating reactions into the additional compartment indicated by MitoCore, while retaining the original reaction in its initial compartment. This approach ensured that potential compartment-specific metabolic activity was represented without constraining flux through existing pathways.

In total, six reactions were duplicated across compartments as part of this curation step. All duplicated reactions were generated using RAVEN's copyToComps functionality, preserving stoichiometry and gene–reaction associations [35]. A summary of duplicated reactions and their corresponding compartments is provided in Appendix Table A.2.

Summary of suggested model updates

Comparison of mitochondrial reactions between MitoCore and HumanGEM revealed

a high degree of overall consistency, with the majority of reactions requiring no modification. Of the 328 MitoCore reactions evaluated, 183 reactions showed agreement in both reaction reversibility and subcellular compartment localization and were therefore retained unchanged in HumanGEM. An overview of reaction matches and mismatches identified during the curation process is provided in Table 2.1.

Discrepancies in reaction reversibility were identified for 85 reactions. Of these, 39 reactions were resolved through updates to reaction bounds in HumanGEM based on thermodynamic evidence derived from estimates of the transformed Gibbs free energy of reaction ($\Delta_r G'_m$). After further testing as described in Section 2.2.2, one of these reactions was reverted to its original bounds. The remaining 46 reversibility mismatches were retained as originally defined in HumanGEM, either because thermodynamic estimates did not support a change in directionality or because insufficient biochemical evidence was available to justify modifying reaction bounds.

A smaller number of discrepancies were observed in subcellular compartment localization, affecting 17 reactions in total. Six of these were resolved by duplicating reactions across compartments to reflect mitochondrial localization supported by MitoCore and independent localization evidence. The remaining compartment mismatches were maintained in their original HumanGEM localization, either because the required metabolites were not present in the proposed compartment in HumanGEM or because available evidence was insufficient to support reassignment or duplication.

Finally, 43 reactions present in MitoCore were identified as missing from HumanGEM (Table 2.1). None of these reactions were added during the curation process. These cases corresponded to reactions that were already represented in HumanGEM but grouped or formulated differently (33 reactions), reactions specific to the MitoCore model scope (5 reactions), or reactions for which there was insufficient biochemical or localization evidence to support their inclusion in HumanGEM (5 reactions).

Overall, the suggested updates reflect a conservative curation strategy in which modifications to HumanGEM were applied only when supported by thermodynamic feasibility or independent biochemical evidence, while reactions lacking sufficient support were retained unchanged to preserve model integrity.

Table 2.1: *Classification and resolution of reaction discrepancies between MitoCore and HumanGEM.*

Discrepancy type	**Total**	**Resolved**	**Retained**
Total MitoCore Reactions Evaluated	328		
Reversibility mismatches	85	38	47
Compartment mismatches	17	6	11
Missing reactions	43	0	43
Fully consistent reactions	183	–	–

2.2.2 Verification of Curation

The curated model was evaluated using RAVEN's `checkTasks` command on the Essential, Verification, and Full metabolic task sets, as defined in the `data/metabolicTasks` directory of the Human-GEM GitHub repository.[1] Implementing the reversibility changes summarised in Appendix Table A.1 initially caused several tasks to fail. Systematic testing showed that retaining reaction MAM03215 as irreversible restored feasibility for all task sets. Consequently, MAM03215 was excluded from the final set of curated reversibility updates.

2.2.2.1 Flux variability analysis (FVA)

To evaluate how the mitochondrial curation affected the solution space of the model, I compared flux variability analysis (FVA) results between the curated model on the `feat/curateMitochondria` branch and the non-curated model from the `develop` branch on GitHub [30]. FVA computes, for each reaction, the minimum and maximum feasible flux values ($v_{\min}$ and $v_{\max}$) while satisfying the steady–state constraint and all imposed bounds [23]. The result is an interval $[\ v_{\min}, v_{\max}\ ]$ describing the range of fluxes compatible with the model constraints for every reaction.

FVA was run for both models and the resulting intervals were compared on a reaction–wise basis. Of the 12 931 reactions that were common to both models, 12 329 reactions (95.3 %) retained identical feasible flux ranges $[\ v_{\min}, v_{\max}\ ]$, while 602 reactions (4.7 %) showed any change in $v_{\min}$, $v_{\max}$, or both. Thus, the vast majority of the network is unaffected at the level of feasible flux ranges.

Within the set of 602 changing reactions, two main patterns were observed. First, a small subset of 38 reactions exhibited large, discrete shifts in their allowable flux. These changes correspond to reactions effectively switching between "off" and "open" states. This includes reactions whose upper bound changed from $v_{\max} = 0$ to $v_{\max} = 1000$ or from $v_{\max} = 1000$ to $v_{\max} = 0$, or whose lower bound changed from $v_{\min} = 0$ to $v_{\min} = -1000$ or from $v_{\min} = -1000$ to $v_{\min} = 0$. Of these 38 reactions, 30 coincide directly with the curated set of reactions whose reversibility bounds were intentionally updated based on thermodynamic evidence (Appendix Table A.1). The remaining eight reactions became feasible in one direction indirectly, through network coupling to the curated reactions. Six of these are transport or exchange reactions, and the remaining two are mitochondrial internal reactions, suggesting that the curated changes propagate mainly through pathways connected to the mitochondrial compartment.

The second, much larger subset of changing reactions showed only modest quantitative adjustments in their FVA bounds. For these reactions the absolute fold-change in the magnitude of $v_{\max}$ (or $v_{\min}$) was close to one (typically |fold_abs| $\approx$ 1.1–1.3), corresponding to changes on the order of 10–30 % in the maximal feasible flux. These alterations can be interpreted as fine–tuning of allowable capacities rather than qualitative switches between active and inactive states.

[1] Human-GEM repository: `SysBioChalmers/Human-GEM` on GitHub.

This behavior is illustrated by scatter plots of the FVA bounds in the curated model versus those in the `develop` model, restricted to the 602 reactions that changed (2.2). Most points lie close to the identity line $y = x$, indicating that for the majority of these reactions the feasible flux ranges are only slightly perturbed. A small number of outliers deviate strongly from this line and correspond precisely to the 38 reactions with large discrete changes described above. Overall, the FVA comparison shows that the mitochondrial curation induces the expected directionality changes in a targeted set of reactions, while preserving the global structure and flux capacity of the rest of the network.

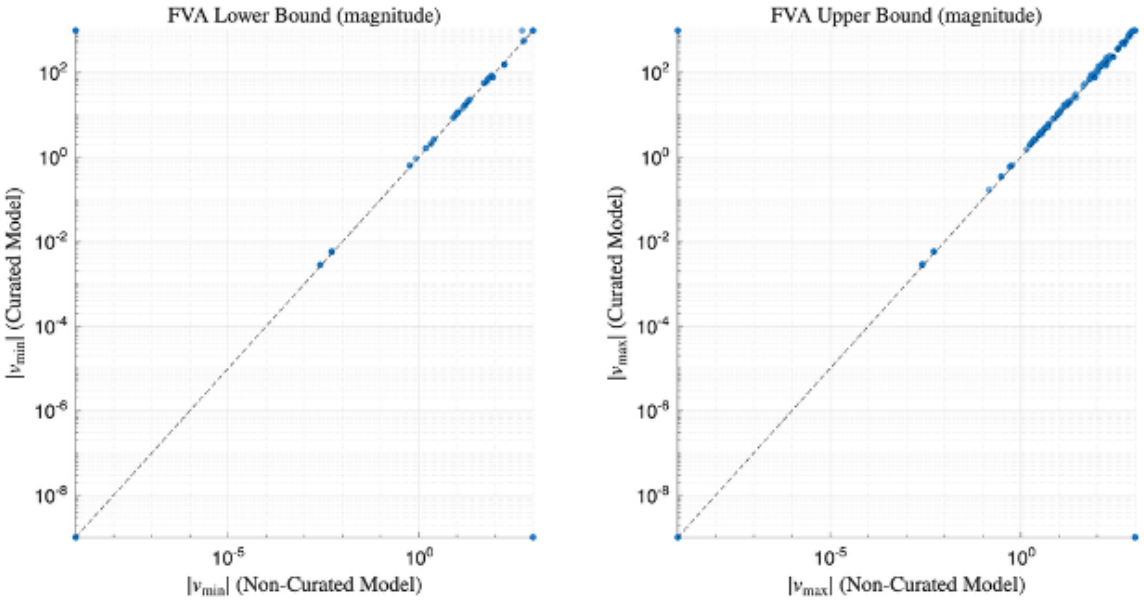

Figure 2.2: ***Comparison of flux variability ranges between the non-curated and curated models.*** *Log–log scatter plots of the absolute FVA bounds for the 602 reactions whose feasible flux ranges changed between the non-curated model and the curated model. (A) Lower bounds $|v_{\min}|$; (B) upper bounds $|v_{\max}|$. The dashed line indicates the identity line y=x. Points close to this line represent reactions with only minor quantitative changes in their feasible flux range, whereas the outliers on the axis correspond to the 38 reactions whose allowable flux was substantially expanded or restricted as a result of the curation.*

3

Patient-Specific GEMs

3.1 Overview of Workflow

An overview of the workflow used to generate and analyze patient-specific genome-scale metabolic models (GEMs) is shown in Figure 3.1. Whole-blood RNA-seq data from participants were integrated with HumanGEM using the ftINIT contextualization algorithm to generate personalized metabolic models for each patient sample [32]. Flux sampling was then performed on each model to explore the feasible metabolic solution space and generate distributions of possible reaction fluxes. Finally, statistical analyses were applied to compare metabolic behavior between diagnosis groups and identify reactions and pathways associated with prodromal PD.

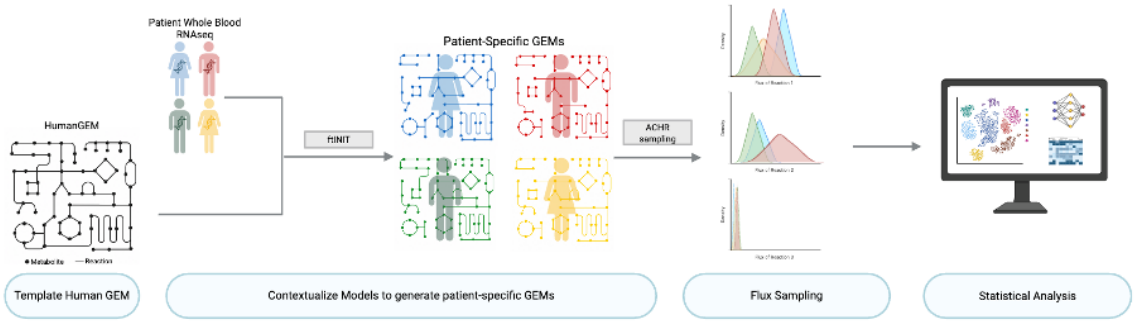

Figure 3.1: *Overview of the workflow used to generate and analyze patient-specific GEMs.*

3.2 Methods

3.2.1 Clinical Cohort and Transcriptomic Data

Clinical and transcriptomic data used in this study were obtained from the Parkinson's Progression Markers Initiative (PPMI), an ongoing longitudinal study focused on identifying biomarkers associated with PD progression [36]. The cohort included healthy controls, individuals with established PD, and individuals classified as prodromal PD based on the presence of prodromal symptoms and associated risk factors.

Whole-blood RNA sequencing (RNA-seq) data were used to generate patient-specific

GEMs. Blood samples were collected longitudinally at baseline (BL), year 1 (Y1), year 2 (Y2), and year 3 (Y3) visits. Samples from each timepoint were analyzed independently to evaluate metabolic changes associated with disease progression over time.

Whole-blood transcriptomic data were used in this project because they provide a minimally invasive and clinically accessible source of molecular information. Although PD is primarily a neurodegenerative disorder affecting the central nervous system, peripheral molecular signatures have previously been reported in blood-based transcriptomic studies of PD and prodromal PD.

3.2.2 Generation of Patient-Specific GEMs

Patient-specific GEMs were generated by integrating whole-blood RNA-seq data with the curated HumanGEM template model using the ftINIT algorithm implemented in the RAVEN toolbox. ftINIT is a task-driven contextualization method that generates context-specific metabolic models by retaining reactions supported by transcriptomic evidence while ensuring that essential metabolic functions remain feasible [32].

Generation of patient-specific GEMs largely followed the workflow and recommendations provided in the Human-GEM contextualization tutorial developed by the SysBioChalmers group [37]. First, the curated HumanGEM model was prepared for ftINIT using the `prepHumanModelForftINIT` function in RAVEN. This preparation step generated a reference structure containing model information, metabolic task definitions, and reaction annotations required for subsequent contextualization. Essential metabolic tasks provided within the Human-GEM repository were used during model preparation to ensure preservation of core metabolic functionality.

Transcriptomic input data consisted of TPM-normalized whole-blood RNA-seq expression values organized as a gene-by-sample expression matrix. Genes with TPM values greater than 1 were considered expressed. Model contextualization was performed independently for each sample using the ftINIT algorithm with the "1+0" initialization settings obtained from the Human-GEM framework. During contextualization, reactions lacking sufficient transcriptomic support could be removed unless required to satisfy essential metabolic tasks. This reaction pruning process generated metabolically functional but transcriptomically constrained patient-specific GEMs representing the metabolic capabilities of individual samples.

In total, 2326 patient-specific GEMs were generated across all diagnosis groups and timepoints. Models were generated using MATLAB together with the RAVEN toolbox and the Gurobi optimizer.

3.2.3 Structural Analysis of GEMs

Following contextualization, structural characteristics of the patient-specific GEMs were evaluated to assess variability in network composition between samples and

disease groups. For each model, the total number of reactions (*nRxns*), metabolites (*nMets*), and genes (*nGenes*) was calculated using the model structures generated by ftINIT. These metrics were compared across diagnosis groups and longitudinal timepoints to evaluate overall differences in model size and network complexity.

To further investigate structural similarity between models, binary reaction presence matrices were generated in which each reaction was encoded as either present (1) or absent (0) within a given patient-specific model. This produced a binary representation of network composition across all samples.

Dimensionality reduction was then applied to the binary reaction presence matrix to visualize relationships between models in lower-dimensional space. Principal component analysis (PCA) and t-distributed stochastic neighbor embedding (tSNE) were performed independently for each longitudinal timepoint using reaction presence profiles as input features. These analyses were used to assess whether patient-specific GEMs clustered according to disease state based on overall network structure.

3.2.4 Flux Sampling

Flux sampling was performed to characterize the feasible flux space of each patient-specific GEM beyond a single optimal FBA solution. Sampling approaches were partially guided by previously published workflows for GEM analysis and flux-space characterization by Beura *et al.* [25]

Sampling was performed using the Artificial Centering Hit-and-Run (ACHR) algorithm implemented in the COBRApy package [38, 22]. Prior to sampling, each patient-specific GEM was loaded into COBRApy and solved using the Gurobi optimizer [39]. Sampling was performed independently for each model using a thinning factor of 100 to reduce autocorrelation. For each model, 5000 feasible flux samples were generated and saved for downstream analysis.

Following sampling, summary statistics including mean, median, standard deviation, minimum, maximum, and interquartile range were calculated for each reaction flux distribution within each patient-specific model. Median flux values were subsequently used for downstream analyses and visualization because they provided a robust summary of the sampled flux distributions while reducing sensitivity to extreme sampled values.

3.2.5 Differential Flux Analysis

Differential flux analysis (DFA) was performed to identify reactions with significantly different sampled flux distributions between diagnosis groups. Median sampled flux values from each patient-specific GEM were used as input for statistical testing. For each reaction, pairwise comparisons were performed between healthy controls, prodromal PD, and PD groups.

Prior to analysis, median reaction flux values from all sampled models were merged

into a reaction-by-model matrix together with associated clinical metadata, including diagnosis group and longitudinal timepoint. DFA was performed independently for each clinical timepoint (BL, Y1, Y2, and Y3).

For each reaction, differences in sampled flux distributions between groups were assessed using two-sided Mann–Whitney U tests [40]. This non-parametric approach was selected because sampled flux distributions did not satisfy assumptions of normality and frequently exhibited skewed or non-Gaussian behavior. Reactions were only tested when at least ten patient-specific models were present in each comparison group.

P-values were adjusted using the Benjamini–Hochberg false discovery rate (FDR) correction method to account for multiple hypothesis testing across reactions [41]. Reactions with FDR-adjusted p-values below 0.05 were considered statistically significant. Median flux differences between groups were additionally calculated for each reaction to evaluate the direction and magnitude of metabolic changes.

No minimum effect-size threshold was imposed during DFA because the analysis was intended to serve as an exploratory systems-level assessment of metabolic alterations associated with disease state. Given the subtle and heterogeneous nature of PD-associated metabolic changes, applying a strict effect-size cutoff could exclude relevant reactions exhibiting modest but statistically consistent shifts across patients. Instead, statistical significance was determined solely using FDR-adjusted p-values, while effect magnitudes were evaluated during downstream biological interpretation.

To improve biological interpretability, DFA was restricted to reactions associated with at least one annotated gene within HumanGEM. Reactions lacking gene associations were excluded from downstream analysis because these reactions often represent transport, exchange, demand, or other mathematically necessary network constraints that are less directly linked to transcriptomic regulation and cellular biological processes.

In addition to performing DFA across all gene-associated reactions within the patient-specific GEMs, a second targeted DFA was performed using only reactions localized to the mitochondrial compartment. This mitochondrial-focused analysis was conducted to specifically investigate mitochondrial metabolic alterations associated with PD while simultaneously reducing the total number of statistical comparisons included in multiple hypothesis correction.

3.3 Results

3.3.1 Cohort Characteristics

Participants in this project were obtained from the Parkinson's Progression Marker Initiative [36]. There were 2326 transcriptomic samples from 681 individuals collected across four longitudinal timepoints.

The cohort consisted of 692 healthy control samples from 196 individuals, 1439 PD samples from 421 individuals, and 195 prodromal samples from 64 individuals. A summary of sample distribution across diagnosis groups and timepoints is provided in Table 3.1.

Diagnosis	**Baseline**	**Year 1**	**Year 2**	**Year 3**	**Total**
Control	189	179	165	159	692
PD	393	354	352	340	1439
Prodromal	58	59	58	20	195
Total	640	592	575	519	2326

Table 3.1: *Distribution of samples across diagnosis groups and timepoints.*

The number of available samples decreased across longitudinal follow-up visits, reflecting incomplete longitudinal sampling and participant attrition over time. PD samples represented the largest proportion of the cohort at all timepoints, while the prodromal group contained fewer samples, particularly at year 3 follow-up.

Demographic distributions across diagnosis groups and longitudinal visits are shown in Figure 3.2. Age distributions were generally comparable between groups across all timepoints, although the prodromal cohort exhibited a slightly older median age. Sex distributions remained relatively consistent across timepoints within each diagnosis group, with male participants representing the slight majority of samples in all cohorts. The prodromal group was slightly more male-dominated than the healthy or PD groups (Figure 3.2).

3.3.2 Structural Characteristics of Patient-Specific Models

Structural characteristics of the patient-specific GEMs were evaluated to assess variability in network composition across diagnosis groups and longitudinal timepoints. The total number of reactions (*nRxns*), metabolites (*nMets*), and genes (*nGenes*) present within each model were compared between healthy control, PD, and prodromal cohorts at each clinical visit.

Overall, patient-specific models exhibited relatively consistent structural properties across diagnosis groups and timepoints (Figure 3.3). While modest variability in model size was observed between individual samples, the distributions of *nRxns*, *nMets*, and *nGenes* remained highly overlapping between disease groups and timepoints.

To further investigate structural similarity between models, t-distributed stochastic neighbor embedding (tSNE) was applied to binary reaction presence matrices generated from the patient-specific GEMs (Figure 3.4a) [42]. Across all longitudinal timepoints, substantial overlap was observed between healthy control, prodromal, and PD samples, with no clear diagnosis-specific clustering patterns apparent in the reduced-dimensional embedding space. Although localized structural clusters were present within the tSNE projections, these clusters contained mixed diagnosis groups rather than disease-specific separations.

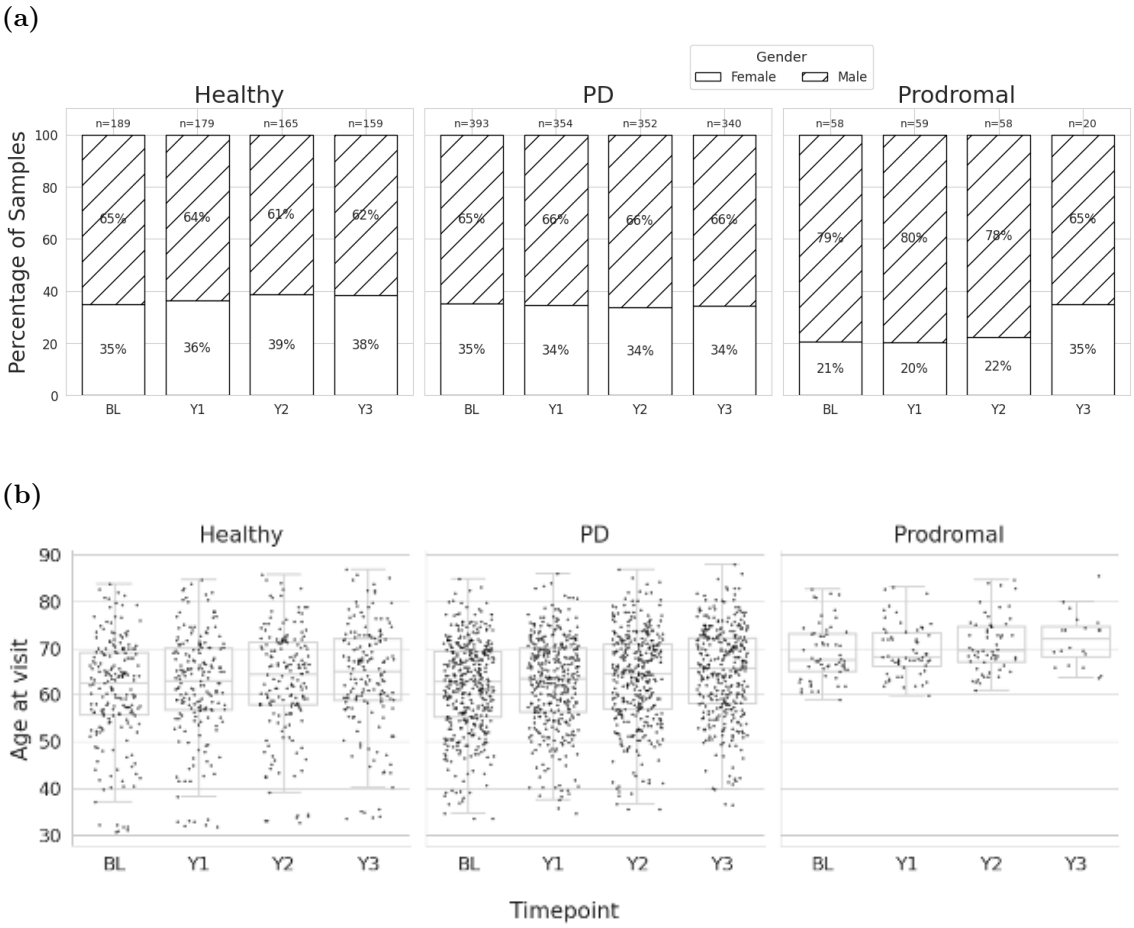

Figure 3.2: ***Demographic characteristics of the study cohort across diagnosis groups and longitudinal timepoints.*** *Panel (a) shows sex distributions within each diagnosis group and timepoint, with bar heights representing the total percentage of samples for each sex and labels above the bars indicate the number of patients in each group. Panel (b) shows age distributions for healthy control, PD, and prodromal cohorts at each timepoint.*

Together, these results suggest that transcriptomic contextualization produced patient-specific GEMs with broadly conserved network structures across cohorts. Principal component analysis (PCA) [43] of the binary reaction presence matrices showed similar patterns of overlap between diagnosis groups and is provided in Appendix Figure B.1.

3.3.3 Flux Space Analysis

To investigate global metabolic behavior across patient-specific GEMs, dimensionality reduction was performed on the median sampled flux distributions generated from flux sampling. For each patient-specific model, median flux values for all sampled reactions were used as input features for tSNE analysis [42].

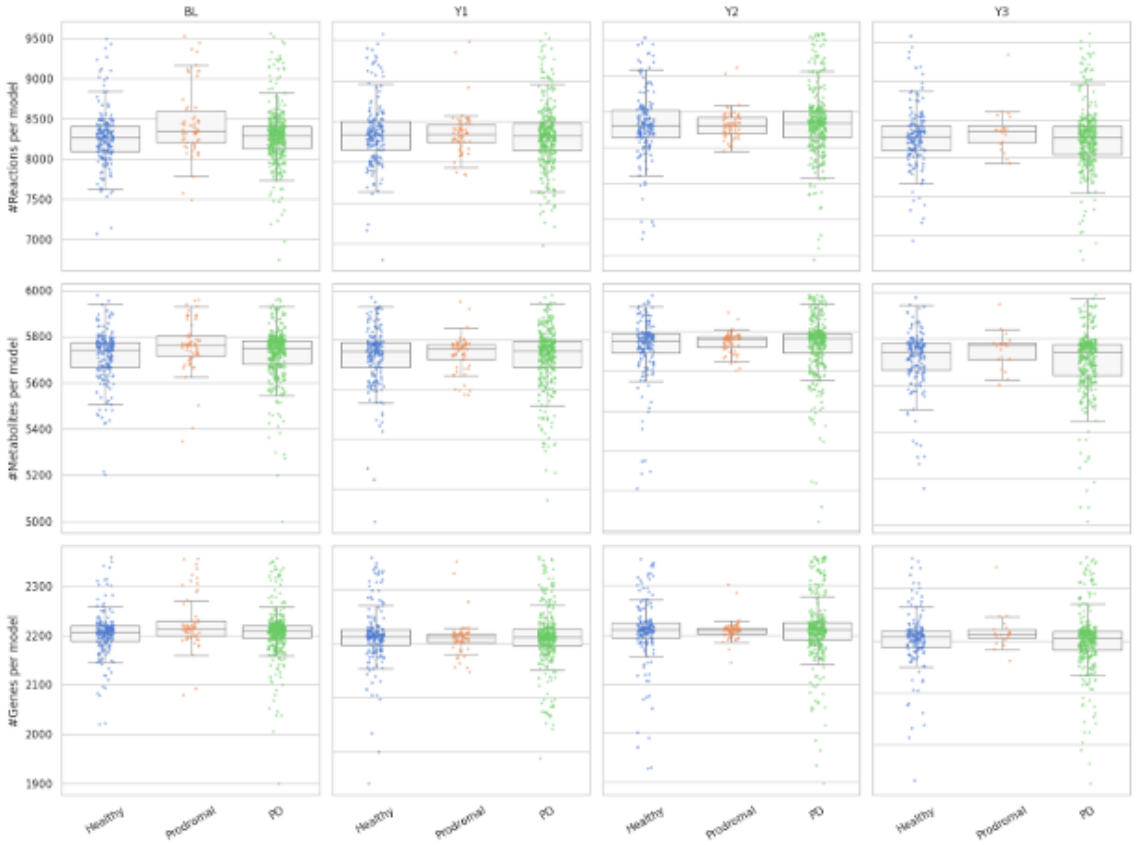

Figure 3.3: *Structural characteristics of patient-specific GEMs across diagnosis groups and longitudinal timepoints. Distributions of the total number of reactions (nRxns), metabolites (nMets), and genes (nGenes) present in each model are shown for healthy control, PD, and prodromal cohorts at each timepoint (BL, Y1, Y2, and Y3).*

The resulting low-dimensional embeddings are shown in Figure 3.4b. Across all longitudinal timepoints, substantial overlap was observed between healthy control, prodromal, and PD samples, with no clear disease-specific clustering patterns apparent within the embedding space. Although localized clustering structures were present, these clusters contained mixed diagnosis groups rather than distinct cohort separations. Similar patterns of overlap were observed across timepoints.

Overall, the flux-space analysis suggested that global metabolic flux states remained broadly similar across diagnosis groups despite inter-individual variability between patient-specific models. PCA of the median sampled flux distributions showed comparable patterns of overlap between cohorts and is provided in Appendix Figure B.2. These findings indicate that disease-associated metabolic differences were not strongly resolved at the global systems level. Consequently, subsequent analyses focused on identifying reaction-level metabolic differences through differential flux analysis rather than relying solely on global flux-space separation.

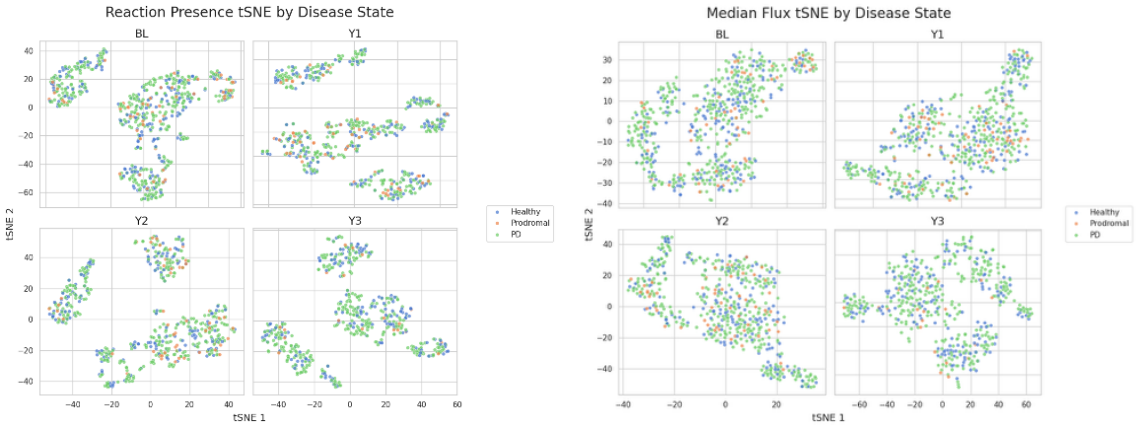

(a) **(b)**

Figure 3.4: *tSNE visualizations of patient-specific GEMs across diagnosis groups and longitudinal timepoints. (A) tSNE projection of binary reaction presence profiles. (B) tSNE projection of median sampled flux distributions generated from flux sampling. Each point represents a single patient-specific model colored according to disease state.*

3.3.4 Differential Flux Analysis

3.3.4.1 Global DFA

Differential flux analysis identified relatively few significantly altered reactions across longitudinal timepoints following FDR correction (Figure 3.5). No significant reactions were identified in the Healthy-vs-PD comparison at any timepoint. In contrast, the largest number of significant reactions was observed at baseline in comparisons involving the prodromal cohort. At baseline, 13 significant reactions were identified in the Healthy-vs-Prodromal comparison and 8 significant reactions were identified in the Prodromal-vs-PD comparison. Notably, all eight reactions identified in the Prodromal-vs-PD comparison at baseline were also significant in the Healthy-vs-Prodromal comparison.

Substantially fewer significant reactions were detected at later longitudinal visits, with only a single significant reaction identified at year 2 and no significant reactions detected at year 1 or year 3 (Figure 3.5). Further information on the individual significant reactions can be found in Appendix Table C.1.

Several of the significant reactions identified by DFA represented sequential metabolic steps with identical sampled flux distributions, indicating tightly coupled flux behavior within specific metabolic pathways. To reduce redundancy in downstream interpretation, these reactions were grouped into flux-coupled reaction groups based on shared metabolic function and flux behavior (Table 3.2). A total of 10 flux-coupled reaction groups were identified, primarily involving pathways associated with fatty acid metabolism, amino acid metabolism, lysosomal degradation, bile acid metabolism, and metabolite transport.

Multiple significant reaction groups were associated with cytosolic fatty acid ac-

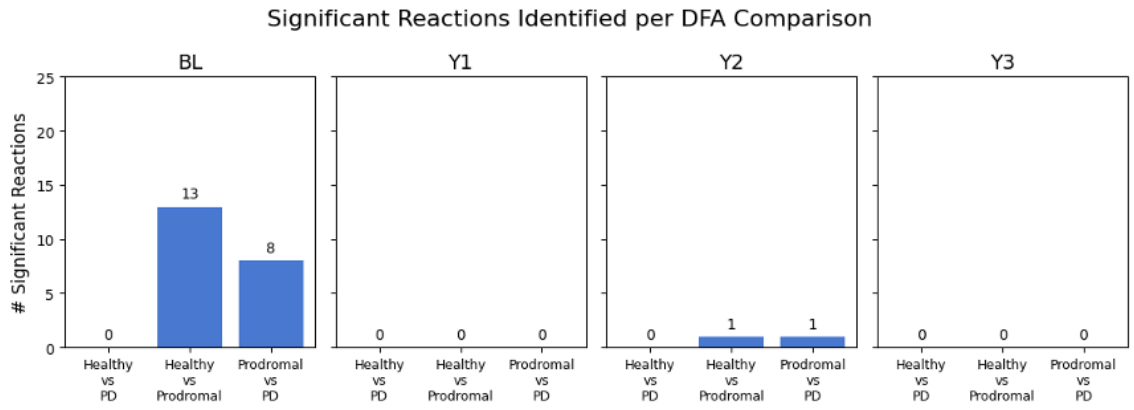

Figure 3.5: *Number of significant reactions identified by DFA at baseline each timepoint using FDR* < 0.05.

tivation and elongation pathways involved in long-chain fatty acid processing and lipid metabolism. Significant flux shifts were also observed in mitochondrial glutamate conversion reactions within arginine and proline metabolism, which are linked to mitochondrial amino acid utilization and redox metabolism. Additional significant reactions were associated with lysosomal keratan sulfate degradation. Several transport-associated reaction groups were also identified, including reactions involved in cAMP export, estradiol glucuronide transport, and estrone sulfate transport.

Estrone sulfate transport was the only reaction identified as significant at the year 2 timepoint and was significant in both the Healthy-vs-Prodromal and Prodromal-vs-PD comparisons. Interestingly, two distinct estrogen conjugate transport reactions were identified as significant across the longitudinal analyses, one at baseline and one at year 2. Both reactions were associated with transport of estrogen conjugates from the extracellular space into the cytosol, although the baseline reaction involved estradiol glucuronide transport whereas the year 2 reaction involved estrone sulfate transport. Notably, the estrone sulfate transport reaction identified at year 2 was also the only significant reaction in which the prodromal cohort exhibited an increase in median sampled flux relative to both healthy controls and PD samples (Figure 3.6).

Representative sampled flux distributions for selected significant reactions are shown in Figure 3.6. Sampled flux values are reported in arbitrary flux units rather than biologically measurable flux rates, since the sampled solution space reflects relative feasible flux distributions constrained by the GEM and transcriptomic inputs rather than experimentally quantified metabolic fluxes. Consequently, interpretation focused primarily on relative shifts in flux distributions between disease groups rather than absolute flux magnitudes.

Across the significant reactions identified at baseline, the prodromal cohort consistently exhibited lower median sampled flux values relative to both healthy controls and PD samples. This pattern was observed across multiple metabolic subsystems.

Despite these statistically significant differences, substantial overlap remained between sampled flux distributions across cohorts, consistent with the limited disease separation observed in the global flux-space analyses. Furthermore, since significant reactions identified through DFA were restricted to a single timepoint, this suggests that the identified metabolic alterations may represent subtle or heterogeneous shifts rather than stable disease-associated metabolic signatures.

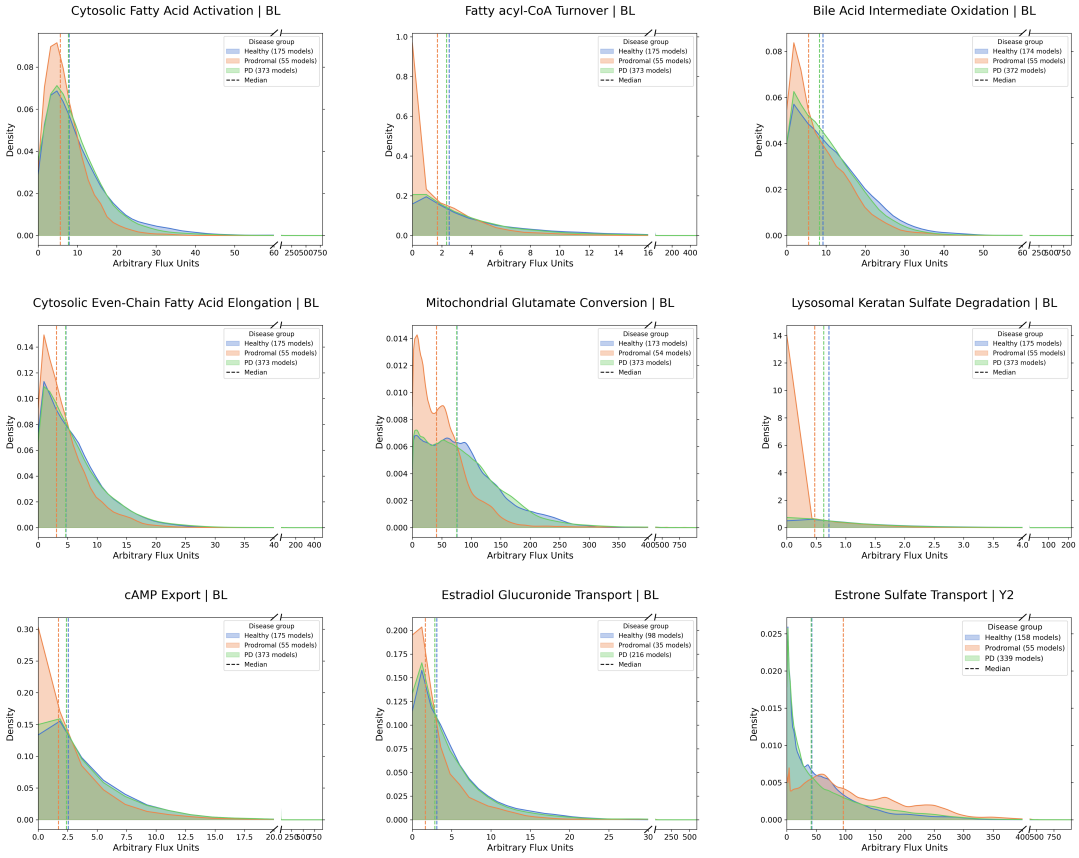

Figure 3.6: *Representative sampled flux distributions for selected flux-coupled reaction groups identified through genome-scale DFA. Each panel displays the sampled flux distribution for a representative reaction from a corresponding flux-coupled reaction group, where all reactions within the group exhibited identical sampled flux distributions. Density plots show model-weighted sampled flux distributions across healthy, prodromal, and PD patient-specific GEMs. Dashed lines indicate group median sampled flux values. The number of models containing each reaction is indicated in the legend for each disease group.*

Flux-Coupled Reaction Group	**HumanGEM Reaction IDs**	**Subsystem**	**Significant Timepoint**	**Significant DFA Comparison(s)**
Cytosolic fatty acid activation	MAR00275	Fatty acid activation (cytosolic)	BL	Healthy-vs-Prodromal; Prodromal-vs-PD
Fatty acyl-CoA turnover	MAR00276	Acyl-CoA hydrolysis	BL	Healthy-vs-Prodromal
Bile acid intermediate oxidation	MAR01681	Bile acid biosynthesis	BL	Healthy-vs-Prodromal
Cytosolic even-chain fatty acid elongation	MAR02211; MAR02212; MAR02213; MAR02214	Fatty acid elongation (even-chain)	BL	Healthy-vs-Prodromal; Prodromal-vs-PD
Mitochondrial glutamate conversion	MAR03895; MAR03897	Arginine and proline metabolism	BL	Healthy-vs-Prodromal; Prodromal-vs-PD
Lysosomal keratan sulfate degradation	MAR07458; MAR07460	Keratan sulfate degradation	BL	Healthy-vs-Prodromal
cAMP export	MAR07691	Transport reactions	BL	Healthy-vs-Prodromal; Prodromal-vs-PD
Estradiol glucuronide transport	MAR09879	Transport reactions	BL	Healthy-vs-Prodromal
Estrone sulfate transport	MAR06129	Transport reactions	Y2	Healthy-vs-Prodromal; Prodromal-vs-PD

Table 3.2: *Flux-coupled reaction groups identified from significant gene-associated reactions in genome-scale DFA. Sequential reactions with identical sampled flux distributions were grouped together.*

3.3.4.2 Mitochondrial DFA

Differential flux analysis restricted to mitochondrial reactions identified a distinct set of significant metabolic alterations relative to the genome-scale DFA (Figure 3.7). In contrast to the global DFA, significant mitochondrial reactions were identified in the Healthy-vs-PD comparison at baseline and year 1. Overall, mitochondrial DFA identified significant reactions at baseline, year 1, and year 2, whereas no significant mitochondrial reactions were detected at year 3.

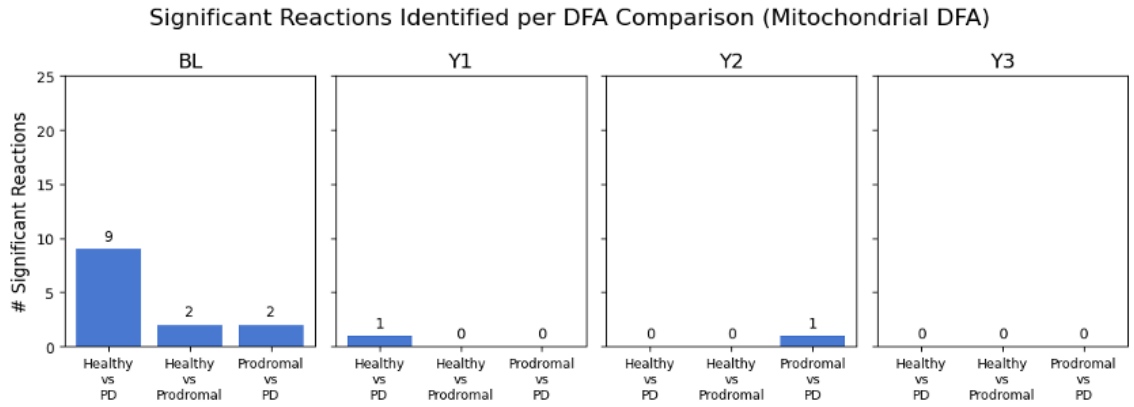

Figure 3.7: *Number of significant reactions identified by DFA within the mitochondrial compartment at each timepoint using FDR* < 0.05.

At baseline, the largest number of significant mitochondrial reactions was observed in the Healthy-vs-PD comparison, where nine significant reactions were identified. However, these reactions were all sequential steps in a singular pathway involved in mitochondrial unsaturated fatty acid β-oxidation (Table 3.3). Additional significant baseline reactions included the mitochondrial glutamate conversion reactions previously identified in the genome-scale DFA, which were significant in both the Healthy-vs-Prodromal and Prodromal-vs-PD comparisons.

At year 1, a single significant reaction associated with the mitochondrial unsaturated fatty acyl-carnitine shuttle was identified in the Healthy-vs-PD comparison. At year 2, a significant glycine transport reaction localized between the cytosol and mitochondrial compartment was identified in the Prodromal-vs-PD comparison. No significant mitochondrial reactions were detected at year 3 following FDR correction.

Similar to the genome-scale DFA, several significant mitochondrial reactions represented sequential metabolic steps with identical sampled flux distributions and were therefore grouped into flux-coupled reaction groups to reduce redundancy in downstream interpretation (Table 3.3). A total of four mitochondrial flux-coupled reaction groups were identified, involving mitochondrial amino acid metabolism, fatty acid β-oxidation, mitochondrial transport processes, and the carnitine shuttle system. More information on the individual significant reactions identified can be found in Appendix Table C.2.

Representative sampled flux distributions for selected mitochondrial reaction groups are shown in Figure 3.8. Compared with the genome-scale DFA, the mitochondrial-

focused analysis identified a distinct set of significantly altered reactions, due to the reduced multiple-testing burden associated with restricting the analysis to mitochondrial reactions. Despite these statistically significant differences, substantial overlap between disease-group flux distributions remained, consistent with the limited disease separation observed in the global flux-space analyses. Overall, these findings suggest that mitochondrial-focused DFA improved the sensitivity for detecting compartment-specific metabolic alterations, although the identified shifts remained relatively modest and heterogeneous across timepoints.

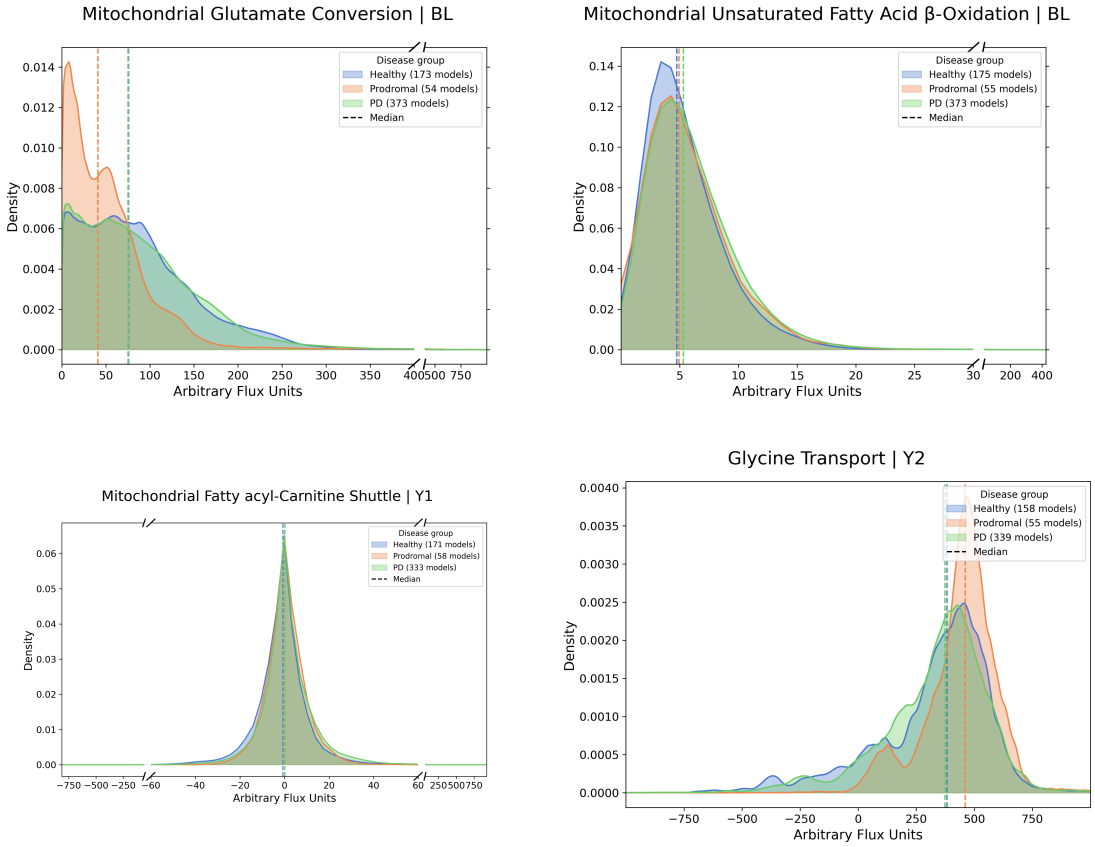

Figure 3.8: *Representative sampled flux distributions for selected flux-coupled reaction groups identified through mitochondrial-focused DFA. Each panel displays the sampled flux distribution for a representative reaction from a corresponding mitochondrial flux-coupled reaction group, where all reactions within the group exhibited identical sampled flux distributions. Density plots show model-weighted sampled flux distributions across healthy, prodromal, and PD patient-specific GEMs. Dashed lines indicate group median sampled flux values. The number of models containing each reaction is indicated in the legend for each disease group.*

Flux-Coupled Reaction Group	**HumanGEM Reaction IDs**	**Subsystem**	**Significant Timepoint**	**Significant DFA Comparison(s)**
Glycine transport	MAR05124	Fatty acid activation (cytosolic)	Y2	Prodromal-vs-PD
Mitochondrial glutamate conversion	MAR03895; MAR03897	Arginine and proline metabolism	BL	Healthy-vs-Prodromal; Prodromal-vs-PD
Mitochondrial unsaturated fatty acid β-oxidation	MAR04978; MAR04984; MAR04988; MAR05001; MAR05083; MAR05090; MAR05177; MAR06281; MAR06320	Fatty acid oxidation	BL	Healthy-vs-PD
Mitochondrial unsaturated fatty acyl-carnitine shuttle	MAR02635	Carnitine shuttle (mitochondrial)	Y1	Healthy-vs-PD

Table 3.3: *Flux-coupled reaction groups identified from mitochondrial-only genome-scale DFA. Sequential reactions with identical sampled flux distributions were grouped together.*

4

Discussion

4.1 Mitochondrial curation of HumanGEM

The first aim of this thesis was to perform a targeted curation of the mitochondrial compartment of HumanGEM through systematic comparison with MitoCore [33]. Although HumanGEM has undergone extensive community-driven development and manual refinement, the mitochondrial compartment had not previously been subjected to a focused reaction-level consistency analysis. Given the central role of mitochondrial dysfunction in PD pathogenesis, improving confidence in the representation of mitochondrial metabolism was considered important prior to downstream patient-specific modeling.

Overall, comparison between HumanGEM and MitoCore demonstrated a high degree of consistency between the two models. Most mitochondrial reactions evaluated required no modification, suggesting that HumanGEM already provides a broadly reliable representation of core mitochondrial metabolism. Nevertheless, a subset of reactions displayed discrepancies in reversibility or compartment localization.

Most of the curated updates involved modifications to reaction reversibility constraints. Reaction directionality is a particularly important property in constraint-based metabolic modeling because it directly defines the feasible solution space available during flux simulations. Incorrectly reversible reactions can introduce thermodynamically infeasible flux cycles, whereas overly restrictive irreversible reactions may artificially constrain biologically feasible pathways. To address this, reaction reversibility decisions were guided primarily using thermodynamic estimates of transformed Gibbs free energy obtained from eQuilibrator together with evidence from MitoCore and biochemical databases [34, 33]. The use of a conservative thermodynamic threshold helped minimize unnecessary modifications while still resolving reactions with strong directional evidence.

Importantly, the majority of curated changes had relatively localized effects on the global network structure. Flux variability analysis demonstrated that more than 95% of reactions retained identical feasible flux ranges following curation, indicating that the overall metabolic capabilities of the model remained largely preserved. Most reactions exhibiting altered FVA ranges showed only modest quantitative changes, while a smaller subset displayed large directional shifts corresponding directly to the

curated reversibility updates. These findings suggest that the curation process successfully introduced targeted mitochondrial refinements without substantially disrupting broader network behavior.

The compartment localization discrepancies identified during comparison with MitoCore also illustrate a common challenge in human GEM reconstruction. Many metabolic enzymes exhibit multi-compartment localization or context-dependent activity, making strict assignment to a single compartment difficult. Rather than removing or relocating existing reactions, discrepant reactions were duplicated across compartments when supported by independent localization evidence from MitoCarta [44]. This conservative approach preserved existing network functionality while expanding the representation of potential mitochondrial metabolic activity.

Overall, the mitochondrial curation performed in this study represents a targeted refinement rather than a large-scale reconstruction effort. The results demonstrate that HumanGEM already captures mitochondrial metabolism with substantial biochemical consistency, while also identifying a limited set of reactions where targeted updates improved agreement with curated mitochondrial biochemistry. These refinements provided a more reliable foundation for the downstream patient-specific metabolic analyses performed in this thesis.

4.2 Patient-specific metabolic modeling and differential flux analysis

The second major aim of this thesis was to investigate whether patient-specific GEMs generated from whole-blood transcriptomic data could identify disease-associated metabolic alterations across healthy, prodromal, and PD cohorts. Although the patient-specific models remained structurally and functionally similar at a structural level, differential flux analysis identified several statistically significant metabolic differences, particularly in comparisons involving the prodromal cohort.

Biological interpretation of Global-DFA

Global model characterization demonstrated minimal separation between diagnosis groups when evaluating reaction presence profiles or sampled flux-space structure. Both tSNE and PCA analyses of binary reaction presence and median sampled flux distributions showed substantial overlap between healthy, prodromal, and PD samples across all longitudinal timepoints. Similarly, structural metrics such as the number of reactions, metabolites, and genes remained highly consistent between diagnosis groups. Together, these findings suggest that whole-blood transcriptomic contextualization did not produce large-scale restructuring of metabolic network architecture between disease states.

The absence of strong global separation is not entirely unexpected given the relatively conserved nature of core human metabolism. Constraint-based contextualization algorithms such as ftINIT are additionally designed to preserve essential

metabolic functionality, meaning that many highly connected housekeeping pathways remain active across all patient-specific models regardless of transcriptomic differences [32]. Furthermore, whole-blood transcriptomic data likely reflects systemic metabolic states rather than neuron-specific metabolic dysfunction, which may reduce sensitivity for detecting disease-associated metabolic changes directly linked to PD neuropathology.

Despite the limited global separation observed in flux-space analyses, DFA identified several significant reaction groups involving lipid metabolism, amino acid metabolism, lysosomal degradation, mitochondrial metabolism, and transport-associated processes. Interestingly, most significant reactions were identified in comparisons involving the prodromal cohort rather than direct Healthy-vs-PD comparisons. In particular, all reactions identified as significant in the Prodromal-vs-PD comparison at baseline were also significant in the Healthy-vs-Prodromal comparison, suggesting that the prodromal cohort may occupy an intermediate or metabolically distinct state relative to both healthy controls and established PD.

Several of the identified reaction groups are biologically relevant to processes previously implicated in PD pathogenesis. Altered fatty acid activation, elongation, and mitochondrial β-oxidation reactions may reflect disruptions in mitochondrial lipid utilization and energy metabolism, both of which have been associated with neurodegenerative disease progression [45, 46]. Similarly, the significant mitochondrial glutamate conversion reactions identified in both the global and mitochondrial-focused DFA analyses may relate to altered amino acid metabolism and mitochondrial redox balance. Multiple studies have shown that imbalance of glutamate levels are implicated in PD pathology [47]. Lysosomal keratan sulfate degradation reactions were also identified, which is notable given the established relationship between lysosomal dysfunction and PD pathology [48].

Transport-associated reactions involving cAMP export and estrogen conjugate transport were additionally identified through DFA. cAMP signaling is involved in multiple neuronal and metabolic regulatory pathways, including dopamine-associated signaling cascades relevant to PD [49]. The identification of two distinct estrogen conjugate transport reactions at different longitudinal timepoints may also be biologically relevant given previous evidence suggesting potential neuroprotective roles of estrogen-associated signaling pathways [**Cattaneo2024**, 50]. Bile acid metabolism has also been found to be altered in both human and animal studies of PD [51, 52, 53].

An important observation across the significant baseline reactions was the consistent reduction in median sampled flux values within the prodromal cohort relative to both healthy controls and PD samples. This pattern was observed across multiple independent metabolic subsystems and may suggest a transient or heterogeneous metabolic state during prodromal disease progression. One possible interpretation is that the prodromal cohort represents a metabolically unstable intermediate state prior to establishment of more compensated metabolic adaptations observed in diagnosed PD patients. However, additional validation using independent datasets

and experimental approaches would be required to support this hypothesis.

Each pathway identified as significant through DFA can be linked to biological processes previously implicated in PD pathology. However, interpretation of these findings should remain cautious, as the identified reactions were all restricted to isolated longitudinal timepoints and exhibited substantial overlap between disease-group flux distributions. Additionally, PD is a highly heterogeneous disease with considerable inter-patient variability in both clinical presentation and molecular pathology [8]. Overall, while the identified metabolic alterations may reflect subtle disease-associated shifts, the results were not sufficiently robust or consistent to support strong disease-specific metabolic signatures.

Biological interpretation of Mitochondrial-DFA

The mitochondrial-focused DFA analysis identified additional significant reactions that were not detected in the genome-scale DFA, particularly within mitochondrial unsaturated fatty acid β-oxidation pathways. Restricting the analysis to mitochondrial reactions reduced the multiple-testing burden associated with FDR correction and may therefore have improved sensitivity for detecting compartment-specific metabolic alterations.

Several of the mitochondrial reaction groups identified through DFA are associated with biological processes previously implicated in PD pathogenesis. The largest mitochondrial flux-coupled group involved reactions associated with mitochondrial unsaturated fatty acid β-oxidation. Mitochondrial fatty acid oxidation is tightly linked to cellular energy production and mitochondrial redox balance, both of which are known to be disrupted in PD [12, 45, 46]. Altered utilization of unsaturated fatty acids has additionally been associated with mitochondrial dysfunction, oxidative stress, and lipid dysregulation in neurodegenerative disease progression [46].

The mitochondrial glutamate conversion reactions identified in both the global and mitochondrial-focused DFA analyses are involved in mitochondrial amino acid metabolism and glutamate utilization, as mentioned above. Glutamate metabolism plays important roles in neurotransmitter balance, nitrogen metabolism, and mitochondrial redox homeostasis, and dysregulated glutamate signaling has been extensively implicated in PD pathology [47]. Interestingly, these reactions were consistently identified in comparisons involving the prodromal cohort, suggesting that altered mitochondrial amino acid metabolism may occur early during disease progression.

Additional significant mitochondrial reactions involved the mitochondrial unsaturated fatty acyl-carnitine shuttle and glycine transport between the cytosol and mitochondrial compartment. Carnitine shuttle systems are essential for transport of long-chain fatty acids into mitochondria for β-oxidation and have previously been linked to mitochondrial dysfunction and altered energy metabolism in PD [12]. Glycine transport may also be biologically relevant given the role of glycine in one-carbon metabolism, redox balance, and mitochondrial metabolic homeosta-

sis. However, compared with the other identified pathways, the direct relationship between altered glycine transport and PD progression remains less well established.

Despite these biologically relevant associations, the identified mitochondrial metabolic alterations remained relatively modest and heterogeneous across longitudinal timepoints. Similar to the genome-scale DFA, substantial overlap persisted between disease-group flux distributions, indicating that these differences likely reflect subtle shifts in feasible metabolic states rather than strong disease-specific mitochondrial signatures.

Overall, this study demonstrates that patient-specific GEMs generated from whole-blood transcriptomic data can identify subtle disease-associated metabolic alterations despite limited global separation between diagnosis groups. The findings highlight potential alterations in mitochondrial and lipid-associated metabolic pathways during prodromal disease stages, while also emphasizing the heterogeneous and complex nature of systemic metabolic dysfunction in PD. However, the identified metabolic differences were relatively modest and lacked sufficient consistency across longitudinal timepoints to support the use of these patient-specific GEMs as a robust standalone approach for early identification of prodromal PD.

4.3 Study Limitations

Several limitations should be considered when interpreting the findings of this study. First, transcriptomic data alone provides only indirect evidence of metabolic activity and does not necessarily correlate with true intracellular flux states. While contextualization algorithms incorporate transcriptomic constraints into GEMs, flux sampling results remain dependent on model structure, imposed constraints, and feasible solution space geometry. Consequently, the sampled flux distributions reported in this thesis should not be interpreted as experimentally measured metabolic fluxes, but rather as relative feasible metabolic states predicted by the model.

Second, all of the significant DFA differences identified in this study were restricted to individual longitudinal timepoints and displayed substantial overlap between disease-group flux distributions. This suggests that the detected alterations represent subtle or heterogeneous metabolic shifts rather than stable disease-specific metabolic signatures.

Another important limitation is the use of whole-blood transcriptomic data for generation of patient-specific GEMs. Although whole blood provides a minimally invasive and clinically accessible sample source, it likely does not fully capture the neuron-specific metabolic alterations underlying PD pathology. The limited separation observed in global flux-space analyses may therefore partially reflect the systemic nature of the transcriptomic input data rather than the absence of disease-associated metabolic dysfunction.

Additionally, GEMs primarily model metabolic processes and therefore do not capture many non-metabolic cellular activities relevant to PD progression, including

protein aggregation, signaling dynamics, neuroinflammation, and other regulatory mechanisms. Since PD is also a highly heterogeneous disease with substantial inter-patient variability in clinical progression and molecular pathology, identifying consistent metabolic signatures across patient cohorts remains inherently challenging.

More broadly, human GEMs also face several limitations associated with modeling multicellular organisms. Unlike microbial GEMs, where biomass maximization often provides a biologically meaningful objective function, there is no universally accepted objective function for human metabolism. As a result, flux predictions in human GEMs may be more sensitive to imposed constraints, contextualization strategies, and sampling approaches.

Finally, several limitations apply specifically to the mitochondrial curation performed in this thesis. The curation primarily focused on reaction reversibility and compartment localization rather than detailed evaluation of stoichiometry, cofactor specificity, or gene–reaction associations. Furthermore, many mitochondrial reactions lacked sufficient thermodynamic or localization evidence to confidently justify modification. In these cases, reactions were intentionally retained unchanged to avoid introducing unsupported assumptions into the model.

4.4 Future directions

Several opportunities exist for extending and improving the approaches used in this thesis. One important future direction would be application of this patient-specific GEM pipeline to other diseases where systemic metabolic dysfunction may be more pronounced or metabolically homogeneous across patients. Similar workflows could potentially be applied to other neurodegenerative diseases, metabolic disorders, or cancer datasets to investigate disease-associated metabolic alterations.

Future studies could also evaluate alternative biological sample sources that may better reflect disease-specific metabolic dysfunction. In particular, cerebrospinal fluid transcriptomics or other central nervous system-associated datasets may provide improved sensitivity for detecting PD-related metabolic alterations compared with whole blood.

Additional improvements could also be made through refinement of model constraints and contextualization strategies. Future analyses may benefit from incorporating more biologically realistic nutrient uptake constraints, ATP maintenance requirements, biomass production constraints, or experimentally informed flux boundaries. Similarly, comparison of multiple contextualization algorithms, including RIPTiDe, INIT, or iMAT, could help determine how contextualization methodology influences downstream flux-space behavior and differential flux analysis sensitivity.

Finally, patient-specific GEMs may have broader future applications in personalized medicine beyond disease characterization alone. For example, personalized metabolic models could potentially be used to predict patient-specific metabolic drug

responses, identify individualized metabolic vulnerabilities, or simulate treatment-associated metabolic adaptations. Although substantial methodological challenges remain, these approaches highlight the potential long-term utility of patient-specific GEMs within precision medicine frameworks.

5

Conclusion

The primary aim of this thesis was to investigate whether patient-specific genome-scale metabolic models generated from whole-blood transcriptomic data could identify metabolic signatures associated with prodromal Parkinson's disease. Overall, the findings did not support the original hypothesis strongly enough to enable clear separation or early identification of prodromal PD patients based on the generated patient-specific GEMs alone. Although several statistically significant metabolic differences were identified, these alterations were generally modest, heterogeneous, and inconsistent across longitudinal timepoints.

Despite this, the smaller aims of the thesis were successfully achieved. A targeted curation of the mitochondrial compartment of HumanGEM was performed through systematic comparison with MitoCore, resulting in improved consistency in reaction reversibility and compartment localization while preserving overall model functionality. In addition, 2326 patient-specific GEMs were successfully generated from longitudinal whole-blood transcriptomic data, representing a large-scale application of transcriptomics-guided metabolic contextualization in PD research.

Differential flux analysis further identified several subtle metabolic alterations associated with lipid metabolism, mitochondrial metabolism, amino acid metabolism, lysosomal pathways, and transport-associated processes, particularly within the prodromal cohort. While these findings were not sufficiently robust for diagnostic applications, they nevertheless provide insight into potential metabolic processes associated with early PD progression and demonstrate the utility of patient-specific GEMs as an exploratory systems biology framework for studying complex disease metabolism.

Bibliography

[1] *Parkinson disease: a public health approach. Technical brief.* Tech. rep. World Health Organization, 2022. URL: https://iris.who.int/server/api/core/bitstreams/90f504c9-c1aa-405a-a16f-ea15eb78ac0d/content.

[2] Ronald B. Postuma et al. "Identifying prodromal Parkinson's disease: Pre-Motor disorders in Parkinson's disease". In: *Movement Disorders* 27 (5 Apr. 2012), pp. 617–626. ISSN: 1531-8257. DOI: 10.1002/MDS.24996. URL: /doi/pdf/10.1002/mds.24996.

[3] Lorraine V. Kalia and Anthony E. Lang. "Parkinson's disease". In: *The Lancet* 386 (9996 Aug. 2015), pp. 896–912. ISSN: 0140-6736. DOI: 10.1016/S0140-6736(14)61393-3. URL: https://www.sciencedirect.com/science/article/pii/S0140673614613933?via%3Dihub.

[4] Dennis W. Dickson. "Neuropathology of Parkinson Disease". In: *Parkinsonism & related disorders* 46 (Suppl 1 Jan. 2017), S30. ISSN: 18735126. DOI: 10.1016/J.PARKRELDIS.2017.07.033. URL: https://pmc.ncbi.nlm.nih.gov/articles/PMC5718208/.

[5] Maria Grazia Spillantini et al. "-synuclein in Lewy bodies [8]". In: *Nature* 388 (6645 1997), pp. 839–840. ISSN: 00280836. DOI: 10.1038/42166;KWRD. URL: https://www.nature.com/articles/42166.

[6] Zoltan Mari and Tiago A. Mestre. "The Disease Modification Conundrum in Parkinson's Disease: Failures and Hopes". In: *Frontiers in Aging Neuroscience* 14 (Feb. 2022), p. 810860. ISSN: 16634365. DOI: 10.3389/FNAGI.2022.810860. URL: https://pmc.ncbi.nlm.nih.gov/articles/PMC8920063/.

[7] Hsiao Chun Cheng, Christina M. Ulane, and Robert E. Burke. "Clinical Progression in Parkinson's Disease and the Neurobiology of Axons". In: *Annals of neurology* 67 (6 June 2010), p. 715. ISSN: 03645134. DOI: 10.1002/ANA.21995. URL: https://pmc.ncbi.nlm.nih.gov/articles/PMC2918373/.

[8] Ullrich Wüllner et al. "The heterogeneity of Parkinson's disease". In: *Journal of neural transmission (Vienna, Austria : 1996)* 130 (6 June 2023), pp. 827–838. ISSN: 1435-1463. DOI: 10.1007/S00702-023-02635-4. URL: https://pubmed.ncbi.nlm.nih.gov/37169935/.

[9] Andrew Siderowf and Anthony E. Lang. "Premotor Parkinson's disease: Concepts and definitions". In: *Movement Disorders* 27 (5 Apr. 2012), pp. 608–616. ISSN: 08853185. DOI: 10.1002/MDS.24954;CSUBTYPE:STRING:SPECIAL;PAGE:STRING:ARTICLE/CHAPTER. URL: /doi/pdf/10.1002/mds.24954%20https://onlinelibrary.wiley.

com/doi/abs/10.1002/mds.24954%20https://movementdisorders.onlinelibrary.wiley.com/doi/10.1002/mds.24954.

[10] Julian M. Fearnley and Andrew J. Lees. "AGEING AND PARKINSON'S DISEASE: SUBSTANTIA NIGRA REGIONAL SELECTIVITY". in: *Brain* 114 (5 Oct. 1991), pp. 2283–2301. ISSN: 0006-8950. DOI: 10.1093/BRAIN/114.5.2283. URL: https://dx.doi.org/10.1093/brain/114.5.2283.

[11] Nicole Exner et al. "Mitochondrial dysfunction in Parkinsons disease: Molecular mechanisms and pathophysiological consequences". In: *EMBO Journal* 31 (14 July 2012), pp. 3038–3062. ISSN: 02614189. DOI: 10.1038/EMBOJ.2012.170,. URL: https://www.embopress.org/doi/pdf/10.1038/emboj.2012.170?download=true.

[12] Martin T. Henrich et al. "Mitochondrial dysfunction in Parkinson's disease – a key disease hallmark with therapeutic potential". In: *Molecular Neurodegeneration 2023 18:1* 18 (1 Nov. 2023), pp. 1–20. ISSN: 1750-1326. DOI: 10.1186/S13024-023-00676-7. URL: https://molecularneurodegeneration.biomedcentral.com/articles/10.1186/s13024-023-00676-7%20http://creativecom-mons.org/publicdomain/zero/1.0/.

[13] A. H.V. Schapira et al. "Mitochondrial Complex I Deficiency in Parkinson's Disease". In: *Journal of Neurochemistry* 54 (3 Mar. 1990), pp. 823–827. ISSN: 14714159. DOI: 10.1111/J.1471-4159.1990.TB02325.X;JOURNAL:JOURNAL:14714159;WGROUP:STRING:PUBLICATION. URL: /doi/pdf/10.1111/j.1471-4159.1990.tb02325.x.

[14] Vincenzo Bonifati et al. "Mutations in the DJ-1 gene associated with autosomal recessive early-onset parkinsonism". In: *Science (New York, N.Y.)* 299 (5604 Jan. 2003), pp. 256–259. ISSN: 1095-9203. DOI: 10.1126/SCIENCE.1077209. URL: https://www.science.org/doi/pdf/10.1126/science.1077209?download=true.

[15] Eriza Maria Valente et al. "Hereditary early-onset Parkinson's disease caused by mutations in PINK1". In: *Science (New York, N.Y.)* 304 (5674 May 2004), pp. 1158–1160. ISSN: 1095-9203. DOI: 10.1126/SCIENCE.1096284. URL: https://www.science.org/doi/pdf/10.1126/science.1096284?download=true.

[16] Derek Narendra et al. "Parkin is recruited selectively to impaired mitochondria and promotes their autophagy". In: *The Journal of cell biology* 183 (5 Dec. 2008), pp. 795–803. ISSN: 1540-8140. DOI: 10.1083/JCB.200809125. URL: https://pubmed.ncbi.nlm.nih.gov/19029340/.

[17] Ines Thiele and Bernhard Palsson. "A protocol for generating a high-quality genome-scale metabolic reconstruction". In: *Nature Protocols* 5 (1 Jan. 2010), pp. 93–121. ISSN: 17542189. DOI: 10.1038/NPROT.2009.203;SUBJMETA. URL: https://www.nature.com/articles/nprot.2009.203.

[18] Changdai Gu et al. "Current status and applications of genome-scale metabolic models". In: *Genome Biology 2019 20:1* 20 (1 June 2019), pp. 121–. ISSN: 1474-760X. DOI: 10.1186/S13059-019-1730-3. URL: https://link.springer.com/article/10.1186/s13059-019-1730-3.

[19] Jeffrey D. Orth, Ines Thiele, and Bernhard O. Palsson. "What is flux balance

analysis?" In: *Nature biotechnology* 28 (3 Mar. 2010), p. 245. ISSN: 10870156. DOI: 10.1038/NBT.1614. URL: https://pmc.ncbi.nlm.nih.gov/articles/PMC3108565/.

[20] Amit Varma and Bernhard O. Palsson. "Metabolic Flux Balancing: Basic Concepts, Scientific and Practical Use". In: *Bio/Technology 1994 12:10* 12 (10 1994), pp. 994–998. ISSN: 1546-1696. DOI: 10.1038/nbt1094-994. URL: https://www.nature.com/articles/nbt1094-994.

[21] Aarash Bordbar et al. "Constraint-based models predict metabolic and associated cellular functions". In: *Nature Reviews Genetics* 15 (2 Feb. 2014), pp. 107–120. ISSN: 14710056. DOI: 10.1038/NRG3643;SUBJMETA. URL: https://www.nature.com/articles/nrg3643.

[22] Jan Schellenberger and Bernhard Palsson. "Use of Randomized Sampling for Analysis of Metabolic Networks". In: *Journal of Biological Chemistry* 284 (9 Feb. 2009), pp. 5457–5461. ISSN: 0021-9258. DOI: 10.1074/JBC.R800048200. URL: https://www.sciencedirect.com/science/article/pii/S0021925820708689?via%3Dihub#bib14.

[23] R. Mahadevan and C. H. Schilling. "The effects of alternate optimal solutions in constraint-based genome-scale metabolic models". In: *Metabolic Engineering* 5 (4 Oct. 2003), pp. 264–276. ISSN: 10967176. DOI: 10.1016/j.ymben.2003.09.002. URL: https://doi.org/10.1128/jb.155.3.1009-1014.1983.

[24] David E. Kaufman and Robert L. Smith. "Direction Choice for Accelerated Convergence in Hit-and-Run Sampling". In: *https://doi.org/10.1287/opre.46.1.84* 46 (1 Feb. 1998), pp. 84–95. ISSN: 0030364X. DOI: 10.1287/OPRE.46.1.84. URL: /doi/pdf/10.1287/opre.46.1.84.

[25] Satyajit Beura, Amit Kumar Das, and Amit Ghosh. "Protocol for genome-scale differential flux analysis to interrogate metabolic differences from gene expression data". In: *STAR Protocols* 5 (3 Sept. 2024), p. 103291. ISSN: 2666-1667. DOI: 10.1016/J.XPRO.2024.103291. URL: https://www.sciencedirect.com/science/article/pii/S2666166724004568?via%3Dihub.

[26] Jonathan L. Robinson et al. "An atlas of human metabolism". In: *Science Signaling* 13 (624 Mar. 2020), p. 1482. ISSN: 19379145. DOI: 10.1126/SCISIGNAL.AAZ1482. URL: /doi/pdf/10.1126/scisignal.aaz1482?download=true.

[27] Adil Mardinoglu et al. "Genome-scale metabolic modelling of hepatocytes reveals serine deficiency in patients with non-alcoholic fatty liver disease". In: *Nature Communications* 5 (1 Jan. 2014), pp. 3083–. ISSN: 20411723. DOI: 10.1038/NCOMMS4083;TECHMETA. URL: https://www.nature.com/articles/ncomms4083.

[28] Ines Thiele et al. "A community-driven global reconstruction of human metabolism". In: *Nature Biotechnology 2013 31:5* 31 (5 Mar. 2013), pp. 419–425. ISSN: 1546-1696. DOI: 10.1038/nbt.2488. URL: https://www.nature.com/articles/nbt.2488.

[29] Natalie C. Duarte et al. "Global reconstruction of the human metabolic net-

work based on genomic and bibliomic data". In: *Proceedings of the National Academy of Sciences of the United States of America* 104 (6 Feb. 2007), pp. 1777–1782. ISSN: 00278424. DOI: 10.1073/PNAS.0610772104;PAGE:STRING:ARTICLE/CHAPTER. URL: /doi/pdf/10.1073/pnas.0610772104?download=true.

[30] SysBioChalmers and Human-GEM contributors. *Human-GEM: The Human Genome-Scale Metabolic Model GitHub*. https://github.com/SysBioChalmers/Human-GEM. 2025.

[31] Daniel Machado and Markus Herrgård. "Systematic Evaluation of Methods for Integration of Transcriptomic Data into Constraint-Based Models of Metabolism". In: *PLOS Computational Biology* 10 (4 2014), e1003580. ISSN: 1553-7358. DOI: 10.1371/JOURNAL.PCBI.1003580. URL: https://journals.plos.org/ploscompbiol/article?id=10.1371/journal.pcbi.1003580.

[32] Johan Gustafsson et al. "Generation and analysis of context-specific genome-scale metabolic models derived from single-cell RNA-Seq data". In: *Proceedings of the National Academy of Sciences* 120 (6 Feb. 2023), e2217868120. ISSN: 10916490. DOI: 10.1073/PNAS.2217868120.

[33] Anthony C. Smith et al. "MitoCore: a curated constraint-based model for simulating human central metabolism". In: *BMC Systems Biology 2017 11:1* 11 (1 Nov. 2017), pp. 114–. ISSN: 1752-0509. DOI: 10.1186/S12918-017-0500-7. URL: https://link.springer.com/article/10.1186/s12918-017-0500-7.

[34] Moritz E. Beber et al. "eQuilibrator 3.0: a database solution for thermodynamic constant estimation". In: *Nucleic Acids Research* 50 (D1 Jan. 2022), pp. D603–D609. ISSN: 0305-1048. DOI: 10.1093/NAR/GKAB1106. URL: https://dx.doi.org/10.1093/nar/gkab1106.

[35] Hao Wang et al. "RAVEN 2.0: A versatile toolbox for metabolic network reconstruction and a case study on Streptomyces coelicolor". In: *PLOS Computational Biology* 14 (10 Oct. 2018), e1006541. ISSN: 1553-7358. DOI: 10.1371/JOURNAL.PCBI.1006541. URL: https://journals.plos.org/ploscompbiol/article?id=10.1371/journal.pcbi.1006541.

[36] Darko Aleksovski et al. "Disease progression in Parkinson subtypes: the PPMI dataset". In: *Neurological sciences : official journal of the Italian Neurological Society and of the Italian Society of Clinical Neurophysiology* 39 (11 Nov. 2018), pp. 1971–1976. ISSN: 1590-3478. DOI: 10.1007/S10072-018-3522-Z. URL: https://pubmed.ncbi.nlm.nih.gov/30109466/.

[37] SysBioChalmers. *Human-GEM Guide: GEM Extraction*. Accessed: 2026-06-05. 2026. URL: https://sysbiochalmers.github.io/Human-GEM-guide/gem_extraction/.

[38] Ali Ebrahim et al. "COBRApy: COnstraints-Based Reconstruction and Analysis for Python". In: *BMC Systems Biology 2013 7:1* 7 (1 Aug. 2013), pp. 74–. ISSN: 1752-0509. DOI: 10.1186/1752-0509-7-74. URL: https://link.springer.com/article/10.1186/1752-0509-7-74.

[39] Gurobi Optimization, LLC. *Gurobi Optimizer Reference Manual*. https://www.gurobi.com. Accessed: 2026-06-08. 2025.

[40] H. B. Mann and D. R. Whitney. "On a Test of Whether one of Two Random Variables is Stochastically Larger than the Other". In: *https://doi.org/10.1214/aoms/1177730491* 18 (1 Mar. 1947), pp. 50–60. ISSN: 0003-4851. DOI: 10.1214/AOMS/1177730491. URL: https://projecteuclid.org/journals/annals-of-mathematical-statistics/volume-18/issue-1/On-a-Test-of-Whether-one-of-Two-Random-Variables/10.1214/aoms/1177730491.full%20https://projecteuclid.org/journals/annals-of-mathematical-statistics/volume-18/issue-1/On-a-Test-of-Whether-one-of-Two-Random-Variables/10.1214/aoms/1177730491.short.

[41] Yoav Benjamini and Yosef Hochberg. "Controlling the False Discovery Rate: A Practical and Powerful Approach to Multiple Testing". In: *Journal of the Royal Statistical Society: Series B (Methodological)* 57 (1 Jan. 1995), pp. 289–300. ISSN: 2517-6161. DOI: 10.1111/J.2517-6161.1995.TB02031.X. URL: /doi/pdf/10.1111/j.2517-6161.1995.tb02031.x%20https://onlinelibrary.wiley.com/doi/abs/10.1111/j.2517-6161.1995.tb02031.x%20https://rss.onlinelibrary.wiley.com/doi/10.1111/j.2517-6161.1995.tb02031.x.

[42] Laurens van der Maaten and Geoffrey E. Hinton. "Visualizing Data using t-SNE". in: *Journal of Machine Learning Research* 9 (2008), pp. 2579–2605. URL: https://api.semanticscholar.org/CorpusID:5855042.

[43] H. Hotelling. "Analysis of a complex of statistical variables into principal components." In: *Journal of Educational Psychology* 24 (6 Sept. 1933), pp. 417–441. ISSN: 00220663. DOI: 10.1037/H0071325.

[44] Sneha Rath et al. "MitoCarta3.0: an updated mitochondrial proteome now with sub-organelle localization and pathway annotations". In: *Nucleic Acids Research* 49 (D1 Jan. 2021), pp. D1541–D1547. ISSN: 0305-1048. DOI: 10.1093/NAR/GKAA1011. URL: https://dx.doi.org/10.1093/nar/gkaa1011.

[45] Melissa Vos et al. "Ceramide accumulation induces mitophagy and impairs -oxidation in PINK1 deficiency". In: *Proceedings of the National Academy of Sciences of the United States of America* 118 (43 Oct. 2021), e2025347118. ISSN: 10916490. DOI: 10.1073/PNAS.2025347118;ISSUE:ISSUE:DOI. URL: /doi/pdf/10.1073/pnas.2025347118?download=true.

[46] Saranna Fanning and Dennis Selkoe. "Parkinson disease is a fatty acidopathy". In: *Nature reviews. Neurology* 21 (11 Nov. 2025), p. 642. ISSN: 17594766. DOI: 10.1038/S41582-025-01142-2. URL: https://pmc.ncbi.nlm.nih.gov/articles/PMC13092291/.

[47] Yan Jun Chen et al. "Glutamate-associated research in Parkinson's disease: a bibliometric analysis". In: *Frontiers in Aging Neuroscience* 17 (2025), p. 1569924. ISSN: 16634365. DOI: 10.3389/FNAGI.2025.1569924. URL: https://pmc.ncbi.nlm.nih.gov/articles/PMC12399607/.

[48] Tim Moors et al. "Lysosomal Dysfunction and -Synuclein Aggregation in Parkinson's Disease: Diagnostic Links". In: *Movement disorders : official journal of the Movement Disorder Society* 31 (6 June 2016), pp. 791–801. ISSN: 1531-8257. DOI: 10.1002/MDS.26562. URL: https://pubmed.ncbi.

nlm.nih.gov/26923732/.

[49] Elena Santini, Emmanuel Valjent, and Gilberto Fisone. "Parkinson's disease: levodopa-induced dyskinesia and signal transduction". In: *FEBS Journal* 275.7 (2008), pp. 1392–1399. DOI: https://doi.org/10.1111/j.1742-4658.2008.06296.xDigitalObjectIdentifier(DOI).

[50] Lisa M. Shulman. "Is there a connection between estrogen and Parkinson's disease?" In: *Parkinsonism and Related Disorders* 8 (5 2002), pp. 289–295. ISSN: 13538020. DOI: 10.1016/S1353-8020(02)00014-7. URL: https://pubmed.ncbi.nlm.nih.gov/15177058/.

[51] Hong Sung Chun and Walter C. Low. "Ursodeoxycholic acid suppresses mitochondria-dependent programmed cell death induced by sodium nitroprusside in SH-SY5Y cells". In: *Toxicology* 292 (2-3 Feb. 2012), pp. 105–112. ISSN: 0300-483X. DOI: 10.1016/J.TOX.2011.11.020. URL: https://www.sciencedirect.com/science/article/pii/S0300483X11005051.

[52] Hayley D. Ackerman and Glenn S. Gerhard. "Bile acids in neurodegenerative disorders". In: *Frontiers in Aging Neuroscience* 8 (NOV Nov. 2016), p. 225062. ISSN: 16634365. DOI: 10.3389/FNAGI.2016.00263/TEXT. URL: www.frontiersin.org.

[53] Kun Nie et al. "Distinct Bile Acid Signature in Parkinson's Disease With Mild Cognitive Impairment". In: *Frontiers in Neurology* 13 (July 2022), p. 897867. ISSN: 16642295. DOI: 10.3389/FNEUR.2022.897867. URL: https://pmc.ncbi.nlm.nih.gov/articles/PMC9289438/.

A

Additional HumanGEM Curation Information

Table A.1: *Mitochondrial reactions with updated lower bound (lb) and upper bound (ub) constraints in HumanGEM based on thermodynamic evidence from eQuilibrator and comparison with MitoCore. Metabolite IDs are denoted in BiGG format where available or in HumanGEM's naming syntax if no BiGG IDs are available. *Reversibility change caused metabolic tasks to fail, so it was not changed in the model.*

HumanGEM ID	Reaction equation	$\Delta_r G'_m$ (kJ mol^{-1})	current_lb	current_ub	new_lb	new_ub
MAR02148	nadp + occoa ↔ MAM00059m + h + nadph	56	-1000	1000	-1000	0
MAR02149	ddcacoa + nadp ↔ dd2coa + h + nadph	56	-1000	1000	-1000	0
MAR02183	tdccoa + nadp ↔ MAM00066m + h + nadph	56	-1000	1000	-1000	0
MAR02187	dcacoa + nadp ↔ dc2coa + h + nadph	56	-1000	1000	-1000	0
MAR04220	hLkynr + h2o + nadp ↔ h + Lkynr + nadph + o2	422	-1000	1000	-1000	0
MAR03809	citr___L + h + pi ↔ cbp + orn	30.3	-1000	1000	-1000	0
MAR03139	3oddcoa + coa → accoa + dcacoa	30.2	0	1000	-1000	0
MAR02207	MAM00053m + h + nadph ↔ MAM02122m + nadp	-56	-1000	1000	0	1000
MAR03806	glu___L + 2 h + nadh ↔ h2o + glu5sa + nad	-50.9	-1000	1000	0	1000
MAR00479	dhap + h + nadh → nad + glyc3p	-22.6	0	1000	-1000	1000
MAR03136	dd2coa + h2o → MAM00174m	0.4	0	1000	-1000	1000
MAR03137	MAM00174m + nad → 3oddcoa + h + nadh	15	0	1000	-1000	1000
MAR03143	dc2coa + h2o → MAM00181m	0.4	0	1000	-1000	1000
MAR03144	MAM00181m + nad → 3odccoa + h + nadh	15	0	1000	-1000	1000
MAR03150	MAM00059m + h2o → MAM00183m	0.4	0	1000	-1000	1000
MAR03151	MAM00183m + nad → MAM00892m + h + nadh	15	0	1000	-1000	1000
MAR03157	MAM00053m + h2o → MAM00182m	-0.7	0	1000	-1000	1000
MAR03158	MAM00182m + nad → MAM00882m + h + nadh	16	0	1000	-1000	1000
MAR03164	b2coa + h2o → 3hbcoa	-3.3	0	1000	-1000	1000
MAR03166	3hbcoa + nad → aacoa + h + nadh	13.8	0	1000	-1000	1000
MAR03213	mmcoa___S → mmcoa___R	0.2	0	1000	-1000	1000
MAR03215*	mmcoa___R → succoa	-8.4	0	1000	-1000	1000

HumanGEM ID	Reaction equation	$\Delta_r G'_m$ (kJ mol^{-1})	current_lb	current_ub	new_lb	new_ub
MAR03744	akg + val___L → 3mob + glu___L	1.7	0	1000	-1000	1000
MAR03753	h2o + 2mp2coa → 3hibutcoa	5.6	0	1000	-1000	1000
MAR03757	3hmp + nad → 2mop + h + nadh	18	0	1000	-1000	1000
MAR03765	akg + leu___L → 4mop + glu___L	0.3	0	1000	-1000	1000
MAR03778	akg + ile___L → 3mop + glu___L	-5.9	0	1000	-1000	1000
MAR03787	acac + succoa → aacoa + succ	12.6	0	1000	-1000	1000
MAR03861	3sala + akg + h → 3snpyr + glu___L	-9.3	0	1000	-1000	1000
MAR03879	hcys___L + ser___L → h2o + cyst___L	-15	0	1000	-1000	1000
MAR03897	glu5p + h + nadph → glu5sa + nadp + pi	-24	0	1000	-1000	1000
MAR04012	adn + atp → adp + amp + h	-15	0	1000	-1000	1000
MAR04288	akg + h + lys___L + nadph → h2o + nadp + saccrp___L	-16	0	1000	-1000	1000
MAR04340	atp + for + thf → 10fthf + adp + pi	-2	0	1000	-1000	1000
MAR04474	6pgc + nadp → co2 + nadph + ru5p___D	-6.8	0	1000	-1000	1000
MAR04656	fol + nadph → dhf + nadp	-10	0	1000	-1000	1000
MAR04667	h2o + nad + saccrp___L → L2aadp6sa + glu___L + h + nadh	16	0	1000	-1000	1000
MAR06768	akg + tyr___L → 34hpp + glu___L	0.4	0	1000	-1000	1000
MAR04190	arg___L + h + nadph + o2 ↔ h2o + nwharg + nadp	N/A	-1000	1000	0	1000

Table A.2: *Reactions duplicated across compartments in HumanGEM based on compartment localization discrepancies with MitoCore. Compartments are denoted as m (mitochondrial) and c (cytosol).*

HumanGEM ID	Original compartment	Duplicated to	Duplicate reaction ID
MAR03802	m	c	MAR020189
MAR03804	m	c	MAR020190
MAR04149	c	m	MAR020193
MAR04336	c	m	MAR020194
MAR06518	c	m	MAR020192
MAR08512	c	m	MAR020191

B

Supplementary Dimensionality Reduction Analysis

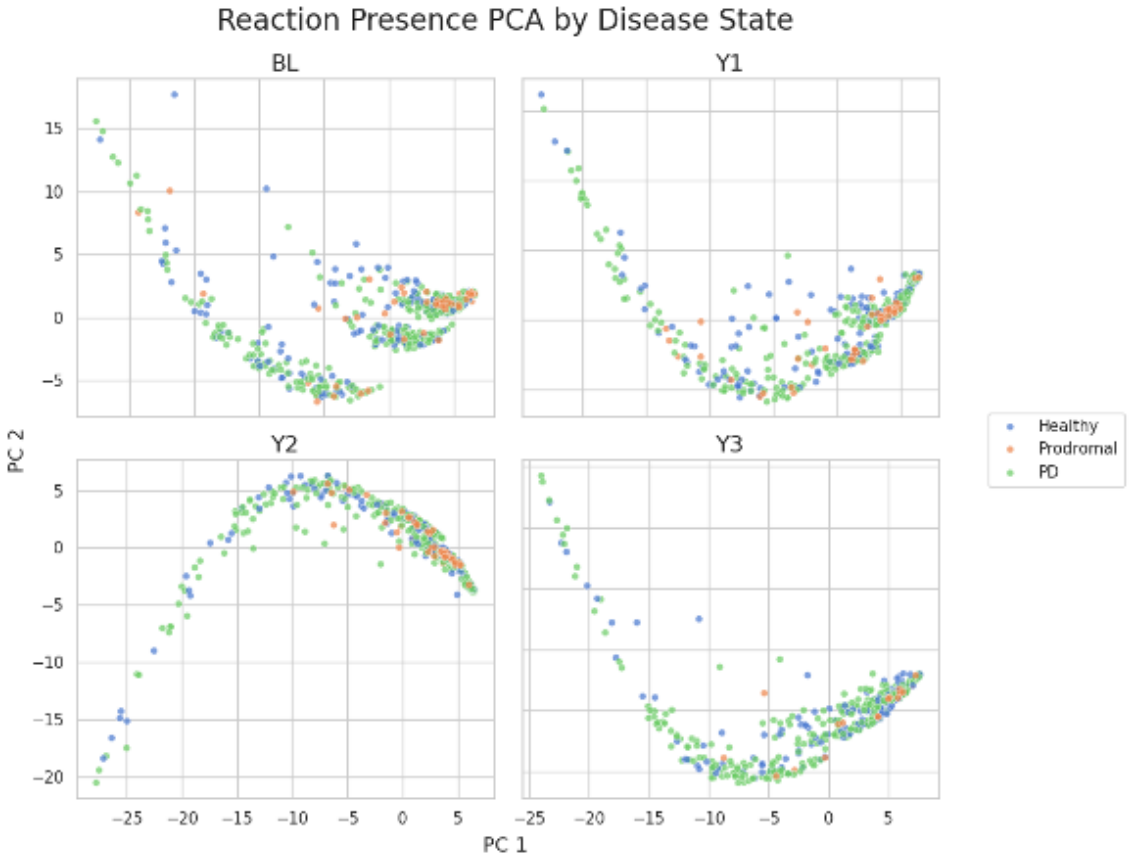

Figure B.1: ***PCA of binary reaction presence profiles*** *across patient-specific GEMs at each longitudinal timepoint. Each point represents a single patient-specific model projected onto the first two principal components (PC1 and PC2) and colored according to disease state (Healthy, Prodromal, or PD). PCA was performed using binary reaction presence matrices derived from the contextualized GEMs.*

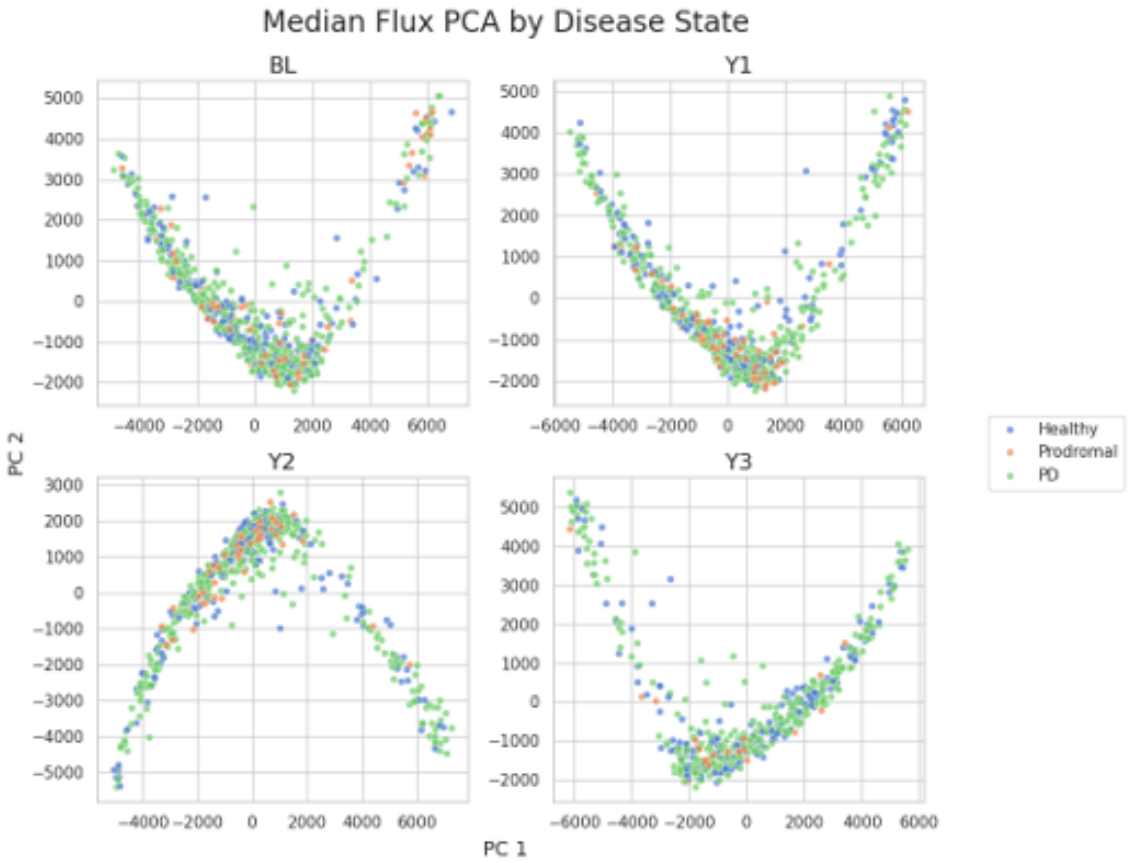

Figure B.2: ***PCA of median sampled flux distributions*** *across patient-specific GEMs at each longitudinal timepoint. Each point represents a single patient-specific model projected onto the first two principal components (PC1 and PC2) based on median reaction fluxes obtained from flux sampling and colored according to disease state (Healthy, Prodromal, or PD). Substantial overlap between diagnosis groups was observed across all timepoints.*

C

Supplementary Differential Flux Analysis Results

Table C.1: *Significant gene-associated reactions identified through genome-scale DFA. Reactions were grouped into flux-coupled reaction groups based on highly similar sampled flux distributions and shared metabolic function.*

HumanGEM ID	Reaction equation	Subsystem	Significant comparison(s)	Timepoint	Compartment	Healthy	Prodromal	PD	Flux-coupled reaction group
MAR00275	lneldc + atp + coa ↔ lneldccoa + amp + ppi	Fatty acid activation (cytosolic)	Healthy-vs-Prodromal; Prodromal-vs-PD	BL	cytosol	175	55	373	Cytosolic fatty acid activation
MAR00276	lneldccoa + h2o ↔ lneldc + coa + h	Acyl-CoA hydrolysis	Healthy-vs-Prodromal	BL	cytosol	175	55	373	Fatty acyl-CoA turnover
MAR01681	xol7ah2 + h + nadph + o2 ↔ xol7ah3 + h2o + nadp	Bile acid biosynthesis	Healthy-vs-Prodromal	BL	cytosol	174	55	372	Bile acid intermediate oxidation
MAR02211	MAM01725c + h + malcoa ↔ MAM00904c + co2 + coa	Fatty acid elongation (even-chain)	Healthy-vs-Prodromal; Prodromal-vs-PD	BL	cytosol	175	55	373	Cytosolic even-chain fatty acid elongation
MAR02212	MAM00904c + h + nadph ↔ MAM00800c + nadp	Fatty acid elongation (even-chain)	Healthy-vs-Prodromal; Prodromal-vs-PD	BL	cytosol	175	55	373	Cytosolic even-chain fatty acid elongation
MAR02213	MAM00800c ↔ MAM00064c + h2o	Fatty acid elongation (even-chain)	Healthy-vs-Prodromal; Prodromal-vs-PD	BL	cytosol	175	55	373	Cytosolic even-chain fatty acid elongation
MAR02214	MAM00064c + h + nadph ↔ nadp + lgnccoa	Fatty acid elongation (even-chain)	Healthy-vs-Prodromal; Prodromal-vs-PD	BL	cytosol	175	55	373	Cytosolic even-chain fatty acid elongation
MAR03895	atp + glu___L ↔ adp + glu5p	Arginine and proline metabolism	Healthy-vs-Prodromal; Prodromal-vs-PD	BL	mitochondria	173	54	373	Mitochondrial glutamate conversion
MAR03897	glu5p + h + nadph ↔ glu5sa + nadp + pi	Arginine and proline metabolism	Healthy-vs-Prodromal; Prodromal-vs-PD	BL	mitochondria	173	54	373	Mitochondrial glutamate conversion
MAR07458	h2o + ksii_core2_deg3 ↔ h + ksii_core2_deg4 + so4	Keratan sulfate degradation	Healthy-vs-Prodromal	BL	lysosome	175	55	373	Lysosomal keratan sulfate degradation
MAR07460	h2o + ksii_core2_deg4 ↔ ksii_core2_deg5 + acgam	Keratan sulfate degradation	Healthy-vs-Prodromal	BL	lysosome	175	55	373	Lysosomal keratan sulfate degradation
MAR07691	atp + camp + h2o ↔ adp + camp + h + pi	Transport reactions	Healthy-vs-Prodromal; Prodromal-vs-PD	BL	extracellular → cytosol	175	55	373	cAMP export
MAR09879	atp + estradiolglc + h2o ↔ adp + estradiolglc + h + pi	Transport reactions	Healthy-vs-Prodromal	BL	extracellular → cytosol	98	35	216	Estradiol glucuronide transport
MAR06129	estrones + hco3 ↔ estrones + hco3	Transport reactions	Healthy-vs-Prodromal; Prodromal-vs-PD	Y2	extracellular → cytosol	159	56	343	Estrone sulfate transport

Table C.2: *Significant gene-associated reactions identified through mitochondrial-only genome-scale DFA. Reactions were grouped into flux-coupled reaction groups based on highly similar sampled flux distributions and shared metabolic function.*

HumanGEM ID	Reaction equation	Subsystem	Significant comparison(s)	Timepoint	Compartment	Healthy	Prodromal	PD	Flux-coupled reaction group
MAR05124	gly ↔ gly	Transport reactions	Prodromal-vs-PD	Y2	c↔m	159	56	343	Glycine transport
MAR03895	atp + glu___L ↔ adp + glu5p	Arginine and proline metabolism	Healthy-vs-Prodromal; Prodromal-vs-PD	BL	m	177	54	377	Mitochondrial glutamate conversion
MAR03897	glu5p + h + nadph ↔ glu5sa + nadp + pi	Arginine and proline metabolism	Healthy-vs-Prodromal; Prodromal-vs-PD	BL	m	177	54	377	Mitochondrial glutamate conversion
MAR04978	fad + dec47dicoa ↔ fadh2 + dectricoa	Fatty acid oxidation	Healthy-vs-PD	BL	m	179	55	377	Mitochondrial unsaturated fatty acid β-oxidation
MAR04984	coa + h2o + nad + 2deddicoa ↔ accoa + h + nadh + octe5coa	Fatty acid oxidation	Healthy-vs-PD	BL	m	179	55	377	Mitochondrial unsaturated fatty acid β-oxidation
MAR04988	3deddicoa ↔ 2deddicoa	Fatty acid oxidation	Healthy-vs-PD	BL	m	179	55	377	Mitochondrial unsaturated fatty acid β-oxidation
MAR05001	h + nadp + dectricoa ↔ nadp + 3deddicoa	Fatty acid oxidation	Healthy-vs-PD	BL	m	179	55	377	Mitochondrial unsaturated fatty acid β-oxidation
MAR05083	coa + h2o + nad + 2dodtricoa ↔ accoa + h + nadh + dec47dicoa	Fatty acid oxidation	Healthy-vs-PD	BL	m	179	55	377	Mitochondrial unsaturated fatty acid β-oxidation
MAR05090	3dodtricoa ↔ 2dodtricoa	Fatty acid oxidation	Healthy-vs-PD	BL	m	179	55	377	Mitochondrial unsaturated fatty acid β-oxidation
MAR05177	coa + fad + h2o + nad + 5tedtricoa ↔ accoa + fadh2 + h + nadh + 3dodtricoa	Fatty acid oxidation	Healthy-vs-PD	BL	m	179	55	377	Mitochondrial unsaturated fatty acid β-oxidation
MAR06281	hexe3coa + MAM00053m	Fatty acid oxidation	Healthy-vs-PD	BL	m	179	55	377	Mitochondrial unsaturated fatty acid β-oxidation
MAR06320	coa + fad + h2o + nad + octe5coa ↔ accoa + fadh2 + h + nadh + hexe3coa	Fatty acid oxidation	Healthy-vs-PD	BL	m	179	55	377	Mitochondrial unsaturated fatty acid β-oxidation
MAR02635	hexde7coa + crn ↔ coa + hdd2crn	Carnitine shuttle (mitochondrial)	Healthy-vs-PD	Y1	m	174	59	338	Mitochondrial unsaturated fatty acyl-carnitine shuttle

DEPARTMENT OF LIFE SCIENCE
CHALMERS UNIVERSITY OF TECHNOLOGY
Gothenburg, Sweden
www.chalmers.se

CHALMERS
UNIVERSITY OF TECHNOLOGY